UNIVERSITAT POLITÈCNICA DE VALÈNCIA

Miguel Ángel Lago Ángel

A new approach for the in-vivo characterization of the biomechanical behavior of the breast and the cornea

2014

Supervisors

Carlos Monserrat Aranda

María José Rupérez Moreno

A new approach for the in-vivo characterization of the biomechanical behavior of the breast and the cornea

Author: MIGUEL ÁNGEL LAGO ÁNGEL

Supervisor: Dr. Carlos Monserrat Aranda
Supervisor: Dr. María José Rupérez Moreno

UNIVERSITAT
POLITÈCNICA
DE VALÈNCIA

DEPARTAMENTO DE SISTEMAS INFORMÁTICOS Y COMPUTACIÓN

October, 2014

The research derived from this doctoral thesis has been partially funded by MINECO (INNPACTO, IPT-2012-0495-300000) through the research project ECTASIA.

The work of Miguel Ángel Lago Ángel to carry out this research and to elaborate this dissertation has been supported by the Spanish Government under the FPU Grant AP2009-2414.

Agradecimientos

Llegando al final del camino, uno se pregunta si ha valido la pena el tiempo y esfuerzo invertido y la respuesta es sí. Desde aquel primer día que empecé esta aventura, hasta el último de ellos, ésta ha sido, sin duda, la experiencia más enriquecedora de mi vida. Todo lo aprendido y todo vivido, son cosas que formarán parte de mí y que siempre recordaré con especial alegría.

El trabajo que hay en estas páginas no es algo individual, pues debo dar las gracias a todas las personas que han influido en él en mayor o menor medida. Ha sido mucha la gente que he tenido el placer de conocer durante estos años y que no han dejado de sorprenderme día a día, empezando por mis dos directores de tesis, Carlos y María José, que han sido mis maestros durante estos años y con los que siempre estaré en deuda por todos los consejos y ayuda que me han aportado, no sólo en el ámbito académico. Pero, sobre todo, por la paciencia que han demostrado en muchas de las discusiones que hemos tenido.

Muchísimas gracias a mis compañeros de trabajo con los que he compartido tantos momentos y anécdotas: Rober, Fer, Sandra, Eliseo, Juanjo, Pablo, Álex y, especialmente, a mi segundo de a bordo y amigo Fran, por la ayuda y consejos que han sido cruciales para que esta tesis saliera adelante.

I would also like to thank Andrew Maidment and, specially, Predrag Bakic for his enthusiastic support this last year and during my stay at the University of Pennsylvania. I could have never thought in a better place to stay.

Finalmente, gracias a mis padres Marina y Jesús y a mi hermano Óscar, además de todos los amigos, viejos y nuevos, que han visto como aquella decisión que hizo que me dedicara a la investigación ha dado por fin sus frutos. Una carrera investigadora que no sé a dónde me llevará a partir de ahora. Es un emocionante misterio, el no saber qué me deparará el futuro, que me intriga y estoy deseando descubrir.

That quite definitely is the answer. I think the problem, to be quite honest with you, is that you've never actually known what the question is.

Deep Thought, The Hitchhiker's Guide to the Galaxy
Douglas Adams

Abstract

The characterization of the mechanical behavior of soft living tissues is a big challenge in Biomechanics. The difficulty arises from both the access to the tissues and the needed manipulation in order to know their physical properties. Currently, the biomechanical characterization of organs is mainly performed by testing *ex-vivo* tissue samples or by means of indentation tests. In the first case, the obtained behavior does not represent the real response of the organ. In the second case, it is only a representation of the mechanical response of the indented areas. The purpose of the research reported in this thesis is the development of a methodology for the *in-vivo* characterization of the biomechanical behavior of two different organs: the breast and the cornea. The proposed methodology allows the *in-vivo* characterization of their biomechanical behavior using medical images.

The research reported in this thesis describes a new approach for the *in-vivo* characterization of the biomechanical behavior of the breast and the cornea based on the estimation of the elastic constants of their constitutive models. This estimation is performed using an iterative search algorithm which optimizes these parameters. The search is based on the iterative variation of the elastic constants of the model in order to increase the similarity between a simulated deformation of the organ and the real one. The similarity is measured by means of a volumetric similarity function which combines overlap-based coefficients and distance-based coefficients.

In the case of the breast, the methodology is based on the simulation of the compression of the breast during an MRI-guided biopsy. The validation was performed using breast software phantoms. Nevertheless, this methodology can be easily transferred into its use with real breasts. In the case of the cornea, the methodology is based on the simulation of the deformation of the human corneas due to non-contact tonometry.

Resumen

La caracterización del comportamiento biomecánico del tejido vivo representa un gran reto en biomecánica. La dificultad radica tanto en el complicado acceso a los tejidos como en su manipulación a la hora de conocer sus propiedades físicas. Actualmente, la caracterización biomecánica de los órganos se realiza utilizando muestras de tejido *ex-vivo* que son sometidas a experimentos de tracción y compresión o mediante tests de indentación. En el primer caso, la respuesta obtenida no representa necesariamente el comportamiento real del órgano. En el segundo caso, sólo es una representación de la respuesta mecánica de la zona estudiada. La investigación presentada en esta tesis tiene como propósito el desarrollo de una metodología para la caracterización *in-vivo* del comportamiento biomecánico de dos órganos diferentes: la mama y la córnea. La metodología propuesta permite la caracterización *in-vivo* de su comportamiento biomecánico específico del paciente utilizando imágenes médicas.

La investigación presentada en esta tesis describe una nueva aproximación para la caracterización *in-vivo* del comportamiento biomecánico de la mama y de la córnea basada en la estimación de las constantes elásticas de sus modelos constitutivos. La estimación se realiza mediante un algoritmo que optimiza estos parámetros. La búsqueda está basada en la variación iterativa de las constantes elásticas del modelo con el fin de incrementar la similitud entre la deformación del órgano simulada y su deformación real. La semejanza se mide mediante una función de similitud volumétrica la cual combina medidas de solape y distancia.

En el caso de la mama, la metodología está basada en la simulación de la compresión de la mama durante una biopsia guiada por resonancia magnética. La validación se realizó utilizando *phantoms* software de mama. Esta metodología se puede trasladar fácilmente a mamas reales. En el caso de la córnea, la metodología se basa en la simulación de la deformación de la córnea humana durante el proceso de tonometría sin contacto.

Resum

La caracterització del comportament biomecànic del teixit viu representa un gran repte en biomecànica. La dificultat ve tant del complicat accés als teixits com de la necessitat de manipulació per tal de conèixer les seues propietats físiques. Actualment, la caracterització biomecànica dels òrgans és realitzada utilitzant mostres de teixit *ex-vivo* o mitjançant proves de tracció i compressió. En el primer cas, la resposta obtinguda no representa necessàriament el comportament real de l'òrgan. En el segon cas, només és una representació de la resposta mecànica de la zona estudiada. La investigació presentada en aquesta tesi té com a propòsit el desenvolupament d'una metodologia per a la caracterització *in-vivo* del comportament biomecànic de dos òrgans diferents: la mama i la còrnia. La metodologia proposta permet la caracterització *in-vivo* del seu comportament biomecànic específic per a cada pacient utilitzant imatges mèdiques.

La investigació presentada en aquesta tesi descriu una nova aproximació per a la caracterització *in-vivo* del comportament biomecànic de la mama i de la còrnia basada en l'estimació de les constants elàstiques dels seus models constitutius. L'estimació es realitza mitjançant un algorisme de cerca iterativa que optimitza aquests paràmetres. Hi està basada en la variació iterativa de les constants elàstiques del model per tal d'incrementar la semblança entre una deformació simulada de l'òrgan i el seu comportament real. La semblança és mesura mitjançant una funció de similitud volumètrica la qual combina coeficients de solapament i de distància.

En el cas de la mama, la metodologia està basada en la simulació de la compressió de la mama durant una biòpsia guiada per ressonància magnètica. La validació es va realitzar utilitzant phantoms virtuals de mama. Aquesta metodologia es pot traslladar fàcilment per usar-se amb mames reals. En el cas de la còrnia, la metodologia es basa en la simulació de la deformació de la còrnia humana durant el procés de tonometria sense contacte.

Contents

Chapter 1

Introduction

The medical industry is moving towards the simulation of the real behavior of human organs. Being able to simulate the mechanical response of the human organs can be useful to determine their reactions in a future intervention. Surgical simulation systems provide surgeons with virtual environments that serve as a guide during an intervention, simulating critical *what-ifs* scenarios. They can also be used to train the skills of the novice surgeons. The big challenge of these systems is to guarantee a simulation as similar as possible to the real behavior of the organ.

Patient-specific biomechanical models are the current tendency in surgical simulation. Being able to provide the surgeon with an accurate and specifically designed model of the organ to be treated can be very helpful for many medical applications such as surgical planning, surgical guidance, image registration, and diagnosis. However, constructing patient-specific models of organs is not

an easy task. The internal and external organs of the body are subjected to many loads that affect their mechanical behavior. Therefore, in order to understand the response of tissue to a given interaction, it is necessary to determine its mechanical properties.

Living organs have the ability to undergo large deformations and, even so, recover the original configuration after a certain period of time. This behavior can be characterized as a biomechanical problem. The European Society of Biomechanics defines the Biomechanic Science as "*the study of forces acting on and generated within a body and of the effects of these forces on the tissues, fluids or materials used for diagnosis, treatment or research purposes*". The inherent heterogeneous composition of the organs, as well as the complexity of their internal structures, confer this type of tissues a high malleability. This makes the modelization of its behavior in a virtual environment very hard. Besides, the high variability among individuals and the difficulty of measuring the mechanical response represents the main challenge.

A trustful biomechanical constitutive model of an organ needs to mimic not only its size and shape but also its mechanical behavior, tissue distribution and interactions with the neighboring tissues. Ideally, all this data must be inferred without any intervention, from medical images like Computerized Tomography (CT) or 3D Magnetic Resonance Images (MRI), thus increasing the difficulty of achieving a realistic physical model for the organs of each patient. Previous works have characterized the mechanical behavior of organs by means of *ex-vivo* experiments. However, these results are not realistic enough since the samples become stiffer due to the fluid loss when they are extracted. There are

also studies that measured the mechanical response of the organs *in-vivo*, with the disadvantage of characterizing it only in some specific points besides needing invasive interventions. Therefore, there is a real need of developing new methodologies that allow the *in-vivo* characterization of the whole organ behavior which make use of medical images, thus avoiding invasive interventions such as open surgery.

This thesis presents a new approach for the *in-vivo* characterization of the biomechanical behavior of two different organs: the breast and the cornea. In particular, a methodology based on the estimation of the elastic constants of the constitutive biomechanical models is proposed for each organ. This estimation is carried out as a parameter optimization problem in which the input parameters are iterated over the given fit function to be minimized. The considered function measures the volumetric similarity, including the internal tissue distribution of all the tissues, between a deformation of the organ simulated by a biomechanical model, and the real response of the organ. Genetic heuristics were applied in order to guide the search algorithm since this type of heuristics are suitable to optimize complex functions that may present many local minima.

1.1 Objectives

The main objective of the work presented in this thesis was to develop a methodology for the *in-vivo* characterization of the biomechanical behavior of the breast and the cornea. Specifically, the methodology was aimed to estimate *in-vivo* the patient-specific

elastic constants of the proposed constitutive models for these organs.

Additionally, from this main objective, several secondary objectives arose.

First of all, in order to quantify the error committed by a biomechanical model in the simulation of the biomechanical behavior of a whole organ, several coefficients for medical image analysis were analyzed. This study involved both overlap-based and distance-based coefficients. The aim was to select the set of coefficients which best quantified this error in order to be used as a fit function in the parameter estimation.

The methodology had to be able to estimate the patient-specific elastic constants of the biomechanical models of the breast and the cornea. To carry out this estimation, an iterative algorithm that searches for the minimum of the proposed fit function by changing the input parameters is needed. This parameter optimization must avoid being trapped in local minima or discontinuities. Therefore, a genetic heuristic approach was selected in order to drive the iterative search algorithm and to find the optimum parameters.

The estimation of the elastic constants of the constitutive biomechanical models chosen for the breast and the cornea was carried out by an iterative search algorithm. The automatic nature of this algorithm requires a realistic simulation as well as the guarantee of the convergence of the finite element method used to simulate the deformations that the organs undergo. Therefore, a study of the impact of the mesh quality in these simulations was performed.

Due to the high complexity of its internal tissue distribution, the study was carried out for the case of the breast

In order to characterize *in-vivo* the biomechanical behavior of the breast tissues, an experiment involving a controlled deformation of the breast had to be chosen. This was the mammographic compression that the breast undergoes during an MRI-guided biopsy. The mammographic compression was modeled as a contact problem. The breast tissues were segmented, meshed and placed between two rigid plates on which a controlled force was applied to compress the finite element mesh. The simulated deformation of the breast was then compared to the real one in order to estimate the elastic constants of the selected model.

In the case of the cornea, another experiment that provided a controlled deformation of the cornea had to be simulated. The images taken from a camera during the non-contact tonometry performed by the Corvis® ST device were used as the target deformation. A comparison of the real and simulated deformation was performed in order to estimate *in-vivo* the elastic constants of the proposed model. Analogously to the breast case, a finite element mesh was constructed and the air jet from the tonometer was applied as a pressure on the cornea surface to get the simulated deformation that was compared to the real one.

1.2 Main contributions

- Two coefficients for medical image analysis that measure the similarity between volumes were selected to compare the organ simulated deformation to the real one: the Jac-

card coefficient, which measures the overlap between two volumes; and the Modified Hausdorff Distance, which is related to the distance between the surfaces of two volumes. These coefficients proved to be suitable to evaluate the error committed by the biomechanical simulation of a physical deformation.

- The mesh quality study carried out on the breast model showed that a mesh created by regular elements provided as good results as a mesh with elements adapted to the internal tissue distribution of the breast. Moreover, the elements of the regular mesh had better quality, easier convergence and faster solver times.

- The biomechanical behavior of the breast was characterized using software breast phantoms with an error under 10%. This was performed by the estimation of the elastic constants of the constitutive equations that govern the behavior of its three main tissues. The proposed methodology can be easily applied to real cases.

- Finally, the methodology was also applied to characterize the biomechanical behavior of the *in-vivo* tissue of the cornea. Taking advantage of the tonometry procedure, the patient-specific elastic constants of a hyperelastic second-order Ogden model were estimated for 24 real corneas of 12 patients with an error under 5%.

1.3 Outline

This dissertation is organized in 6 chapters, starting with the introductory Chapter 1, which includes the objectives and main contributions of this thesis.

In Chapter 2, the background and context where the thesis is framed is detailed, including a literature review on characterization of the breast, and the corneal tissues.

Chapter 3 establishes the base of the methodology for the *in-vivo* characterization of the biomechanical behavior of the two organs, including the biomechanical modeling, the description of the genetic heuristics, and the presentation of the similarity coefficients.

Chapter 4 describes the application of the methodology to the breast tissues and its validation using software phantoms. In this chapter, the breast anatomy is detailed along with both the selected constitutive model, and the software phantoms. This chapter also includes the study of the mesh quality.

In Chapter 5, the application of the methodology to real corneas is described. The cornea anatomy and the biomechanical modeling of the tonometry procedure are detailed, as well as the process developed to estimate the elastic constants of the constitutive model that describes the cornea behavior.

Finally, Chapter 6 presents the final conclusions of this dissertation, the future work, and the resulting publications.

Chapter 2

Context and background

This chapter reviews previous works on the biomechanical characterization of soft tissue. Specifically, the literature about the characterization of the breast and the cornea is detailed in order to establish the framework of this thesis.

2.1 Introduction to tissue characterization

In 1972, Fung proposed what is considered the first theory that describes the phenomenological temporal mechanics of the soft tissue. This theory, called the quasi-linear viscoelastic theory, separates the mechanical behavior of the tissue in two components: the nonlinear time-independent hyperelastic component and the linear time-dependent component. This model reduces the formulation of the mathematical model easing the simulation on a computer and, specifically, allowing methods like the Finite

Element Method (FEM), to simplify its resolution.

First steps in biomechanical characterization of human tissue can be found in early 70's. The first experiments performed uniaxial tensile tests to obtain the mechanical response of soft tissues [Clark, 1973; Ghista and Rao, 1973; Lanir and Fung, 1974]. In a tensile test, the sample is gripped by the so-called clamps and a force is applied in order to measure the force feedback caused by the tension. The measured force can be used to infer tissue properties like elasticity or compressibility. However, uniaxial tensile tests are not accurate enough to completely estimate the anisotropic behavior of the soft tissue [Fung, 1974; Chew et al., 1986; May-Newman and Yin, 1995; Billiar and Sacks, 2000; Zhao et al., 2011].

Moving on to more complex tissues, those which have an anisotropic behavior need different experiments like biaxial tensile tests. In this type of tests, the sample is subjected to two forces in different directions, thus obtaining two reactions that allows the characterization of the tissue anisotropy. However, as with uniaxial tests, the characterization is limited to the considered portion of tissue [Nielsen et al., 2002]. Furthermore, the inhomogeneity of biological tissue causes this type of tests to characterize the average behavior of the collected sample, or the region subjected to the stress.

Nowadays, there is an increasing interest in characterizing the biomechanical behavior of the living tissues since, due to the water loss, the *ex-vivo* samples becomes stiffer and their mechanical properties vary significantly. It is also important to highlight the

difficulty of extracting samples of some specific tissues from the body as well as the severe impact that the extraction of the tissues could have on a patient. Additionally, the variability among samples (for different patients and for the same patient in different times), and the inherent conditions of the measuring techniques entail the necessity of creating more specific models for each patient [Gee et al., 2010; Miller and Lu, 2013]. In this direction, works like [Carter et al., 2001; Samur et al., 2005; Nava et al., 2008] performed *in-vivo* indentation tests on animal organs thus measuring their specific mechanical properties.

In an indentation test, a force is applied on a small region of the tissue and the material properties are determined by measuring the force feedback [Gow and Vaishnav, 1975; Hori and Mockros, 1976; Zheng and Mak, 1996; Han et al., 2003; Samani and Plewes, 2004]. As well as with tensile tests, the viscoelasticity, time-dependent response of the tissue, can be determined by these tests [Humphrey et al., 1991; Samani and Plewes, 2004; O'Hagan and Samani, 2009; Martínez-Martínez et al., 2013a]. The anisotropy of the tissue can also be obtained by means of using an asymmetric indentation device [Jeffrey, 2004] as well as the characterization of fiber-reinforced materials [Cox et al., 2008]. However, the problem with all these tests is that they only characterize the biomechanical properties of the small area where the device is applied, with the result of being only valid for that region and not necessarily representing the behavior of the whole organ.

2.2 Characterization of the breast tissues

The simulation of the mechanical behavior of the breast is becoming a very relevant field in the last years owing to its main role in an important number of biomedical applications related to surgical simulations [Tanner et al., 2006a; del Palomar et al., 2008; Hsu et al., 2011; Solves Llorens et al., 2012], surgical guidance [Carter et al., 2008; Han et al., 2011] or cancer diagnosis [Ruiter et al., 2006; Pathmanathan et al., 2008; Rajagopal et al., 2010]. These applications involve large deformations of the internal tissues of the breast such as mammographic compression or gravity loading deformation, which are usually modeled using the Finite Element Method (FEM).

One of the main challenges when modeling the biomechanical behavior of organs like the breast is to create patient-specific models that improve the realism and accuracy in a reasonable computational time. However, the estimation of the biomechanical properties of the living tissues is not straightforward. The measurement of these properties is usually a complex task since the behavior of the tissues is highly variable among individuals. In the case of the breast, there are mainly four tissues whose behavior must be modeled, namely: skin, fat, glandular tissue and the Cooper's ligaments. Each of them has its own biomechanical properties that must be estimated for each patient in order to build an accurate model of the whole breast. In the case of the Cooper's ligaments, since they are not visible in any image scanner modality, its influence on the breast is usually considered implicitly in the fat tissue.

The behavior of the breast tissue has already been measured with *ex-vivo* experiments by indentation or aspiration tests [Gefen and Dilmoney, 2007; O'Hagan and Samani, 2009]. Unfortunately, the behavior of the samples outside the body is more rigid and it does not correspond to the mechanical properties of the living organ.

Elastography is a common method for the *in-vivo* estimation of the elasticity of the breast [Ophir et al., 1991; Krouskop et al., 1998; Greenleaf et al., 2003; Mariappan et al., 2010; Barr, 2012]. This technique measures the dynamic stiffness of a tissue by cyclically applying a load. Despite classic elastography is only useful to estimate the behavior of the tissues when they are considered isotropic and linear elastic, its application to measure the viscoelasticity and the hyperelasticity of the different breast tissues has been reported [Sinkus et al., 2005; Mehrabian et al., 2010]. However, this methodology is not suitable to build a constitutive model able to describe the biomechanical behavior.

In contrast, computational methods based on parameter optimization are being applied to characterize the biomechanical behavior of the tissues *in-vivo*. Specifically, evolutionary computation has been used in this field to identify the elastic constants of a hyperelastic model proposed to characterize the biomechanical behavior of the heart [Pandit et al., 2005; Nair et al., 2007] and also of the arterial wall [Harb et al., 2011]. In [Martínez-Martínez et al., 2013b], our group presented a study based on evolutionary algorithms for the *in-vivo* characterization of the biomechanical behavior of the liver. The conclusion was that genetic algorithms performed better than other algorithms to estimate the elastic con-

stants of any arbitrary biomechanical model proposed to simulate the liver behavior. The main advantage of this approach is the use of medical images which avoids the invasive measure of the mechanical response of the organ.

In the case of the breast, the work presented by Han et al., 2012 characterized the *in-vivo* biomechanical behavior of the internal tissues of the breast by means of an optimization algorithm over medical images of the breast subjected to a controlled compression. The elastic constants of the proposed model were provided by measuring the similarity to a simulation of that compression by changing the model iteratively. This is the first work that used evolutionary computation as a heuristic in an iterative search of the elastic constants that characterize the biomechanical behavior of the breast tissues. The authors used the Normalized Mutual Information (NMI) as a cost function to measure the similarity during the iterative search [Studholme et al., 1999]. However, despite this novel approach, using this image-based comparison may result in inaccurate results since NMI does not consider the spatial distribution of the tissues but only the gray value entropy of both 3D images. In order to evaluate the accuracy of the given model, the cost function must consider the whole volume including the internal tissue distribution.

The methodology presented in this thesis is able to characterize the biomechanical behavior of the breast by means of medical images under a controlled compression. Unlike previous works, the error committed was measured by similarity coefficients considering all the internal tissue distribution of the breast.

2.3 Characterization of the corneal tissue

The case of the cornea is especially complex since not only does it show a great variability between individuals but also a strong sensitivity to age or temperature, thus conditioning its mechanical properties and, therefore, its characterization [Elsheikh et al., 2007]. Being able to estimate *in-vivo* the mechanical response of the cornea can allow the detection of some pathologies whose symptoms can change its stiffness [Hjortdal, 1995]. Moreover, the estimation of the mechanical behavior of the cornea is the core of the analysis of the real response during surgical interventions [Deenadayalu et al., 2006; Lanchares et al., 2008; Gefen et al., 2009; Pandolfi et al., 2009; delBuey et al., 2010].

In [Alastrué et al., 2006], the authors stated that a biomechanical study before refractive corneal surgery is very helpful in quantitatively assessing the effect of each parameter on the optical outcome. In their work, a mechanical model of the human cornea was proposed and implemented under a finite element context to simulate the effects of some common surgical procedures such as photorefractive keratectomy (PRK) and limbal relaxing incisions (LRI). The model considered a nonlinear anisotropic hyperelastic behavior of the cornea. The authors evaluated the effect of the incision variables on the change of curvature of the cornea to correct myopia and astigmatism. They concluded that the model reasonably approximated the corneal response to an increasing pressure. They also showed that tonometry underestimates the value of the intraocular pressure (IOP) after PRK or LASIK surgery.

First works in biomechanical characterization of the corneal

tissue were performed with *ex-vivo* tensile tests [Wollensak et al., 2003; Ahearne et al., 2007; Boyce et al., 2007]. However, the variability between individuals as well as the inherent conditions of the different techniques result in a wide range of elastic parameters [Zeng et al., 2001; Elsheikh et al., 2007]. In order to get an accurate biomechanical model of the cornea, its mechanical behavior must be characterized *in-vivo* and must be patient-specific.

The ORA device (Ocular Response Analyzer) is one of the most commonly known devices for obtaining the IOP along with the corneal hysteresis and the corneal resistance factor, which are a representation of the viscoelasticity of the cornea. The ORA results have been applied to obtain the relationship among the hysteresis, IOP, glaucoma, keratoconus, or aging [Luce, 2005; Kotecha et al., 2006; Shah et al., 2007]. However, hysteresis does not characterize completely the biomechanical behavior of the cornea. In [Glass et al., 2008], the ORA device was used to estimate a viscoelastic biomechanical model of the cornea. By attaching a camera to the device, the authors validated the proposed model using a contact lens as a cornea model. However, as the authors stated, the proposed methodology was able to determine changes or variability in the elasticity of the cornea but could not estimate the biomechanical behavior of the cornea.

In 2011, OCULUS Corvis® ST (OCULUS Optikgeräte GmbH, Müncholzhäuser Str. 29 D-35582 Wetzlar, Germany) was presented (Figure 2.1). This tonometer and pachymeter incorporates a high-speed camera which is able to record the movement of the cornea when applying a controlled force by an air jet. This device is able to measure the IOP and the corneal thickness. Addition-

Figure 2.1: *Corvis ® ST device*

ally, it provides the images of the 1st and 2nd applanation of the cornea as well as a complete ultra-high-speed video of the corneal deformation.

The Corvis® ST applies an air jet at the center of the eye to measure the IOP while a light illuminates the eye and a high-speed camera records the cornea deformation. The air jet is increased by time while the shape of the cornea changes from the initial status (convex) to a maximum deformation status (concave) and then back to the initial status. The light falls upon on a sectional plane of the cornea during the air jet. The cornea scatters the light so that the sectional plane reflection is captured by the camera at an angle of 45°. The video sequence records the deformation of the cornea during the application of the air jet as shown in Figure 2.2. The device measures the IOP by dividing the amount of air pressure into the area of applanated surface using the Imbert-Fick law as a Goldmann tonometer [Goldmann and Schmidt, 1957].

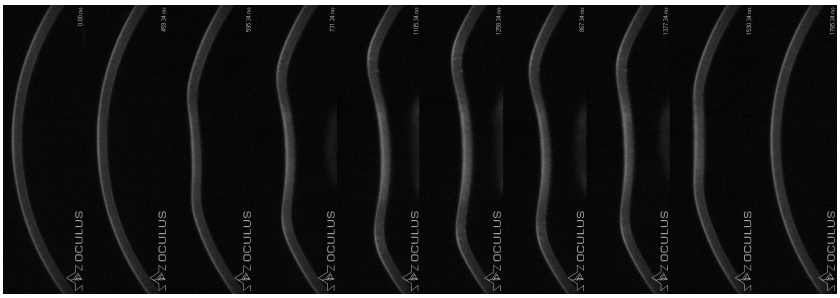

Figure 2.2: *Video sequence taken by the Corvis® ST high-speed camera.*

The Corvis® ST has been approved by the US Food and Drug Administration as a tonometer and pachymeter but not for biomechanical applications. However, the images and video provided by this device can be used to obtain the patient-specific biomechanical response of the human cornea *in-vivo*. Specifically, the work presented in this thesis uses, for the first time, the images of the deformed and undeformed cornea in order to find the elastic constants of the constitutive modelthat characterize the biomechanical behavior of the cornea of each patient.

2.4 Conclusions

The literature related to characterization of soft tissue was reviewed in this chapter, paying special attention to the breast and cornea. Works that characterized the *ex-vivo* and *in-vivo* tissue behavior by indentation tests were presented. These works present several inconveniences such as the need of an invasive intervention to reach the organ or the difficulty of measuring the behavior of the whole organ. Therefore, it is necessary to explore solutions based on medical images like the proposed in this thesis.

Chapter 3

Materials and methods

This chapter details the methods that forms the core of the research developed in this thesis. Basic concepts of Biomechanics and the chosen constitutive models are described. Also, the theory of genetic heuristics is detailed since it plays a major role in the methodology developed to estimate the elastic constants of the constitutive models. Finally, the similarity coefficients which compute the cost function to be minimized by the genetic algorithm are presented. These similarity coefficients allow the comparison between a real and a simulated deformation of the organ. For that reason, an analysis of their performance is also presented in this chapter.

3.1 Biomechanical modeling of soft tissue

As commented in Chapter 2, the mechanical behavior of biological tissue has been widely studied in the literature [Lanir, 1979; Fung, 1993; Provenzano et al., 2002; Kim and Srinivasan, 2005; Gefen and Dilmoney, 2007; Cox et al., 2007; Samani and Plewes, 2007; Shi et al., 2008; Rajagopal et al., 2008; Lanchares et al., 2008; Vigneron et al., 2010; Harb et al., 2011; Tanner et al., 2011; Hsu et al., 2011; Han et al., 2012; Solves Llorens et al., 2012; Martínez-Martínez et al., 2012; Zhang et al., 2013; Burkhart et al., 2013]. In order to generate a reliable and realistic model of the biomechanical behavior of soft tissue, the elastic constants of the constitutive models that govern such behavior need to be obtained. Each type of tissue of the human body has its own biomechanical properties, being also very variable among individuals and with high sensibility to agents like age and environment.

Mainly, the soft tissue behavior can be modeled by one of these models:

- Linear elastic model: the simplest model; it considers a linear relationship between stress and strain. Accurate enough for small deformations.
- Non-linear elastic model (hyperelastic): the relationship between stress and strain is non-linear. It can model large deformations.
- Viscoelastic model: this model considers both viscous and elastic behavior. Viscoelastic materials have a stress-strain relationship dependent on time.

Anisotropy is also considered in many models of the human tissues. In contrast with the isotropic behavior, anisotropic tissues present a different mechanical response depending on the orientation. Finally, human tissues are considered incompressible since they are mainly composed of water. For modeling the biomechanical response of the considered tissue, the most common numerical technique is the finite element method (FEM).

3.1.1 Finite Element Method

The Finite Element Method discretizes a continuous body into multiple subvolumes called elements. This method assumes that the behavior of the continuous body is approximated by the behavior of the entire set of elements. Thus, the solution given by the FEM is an approximation of the real solution whose realism will be directly proportional to the number of elements. The division of the continuum space in small and finite parts is a very common approach on numeric analysis. The set of nodes and elements that results of the discretization of the space is the finite element mesh. The relationship between elements position and their respective coordinates in the continuous space is represented by the so-called shape functions.

For each element e, the displacement vector of any point of the continuous space $\mathbf{u}$ can be approximated to a vector $\tilde{\mathbf{u}}$ that can be calculated using the shape functions $\mathbf{N}$, thus obtaining the nodal displacements of that element $\mathbf{a}^e$.

$$\mathbf{u} \approx \tilde{\mathbf{u}} = \mathbf{N}^e \cdot \mathbf{a}^e \tag{3.1}$$

All displacements $\mathbf{a}^e$ are calculated for the whole element set. Then, the strains can be obtained as Eq. 3.2 shows.

$$\epsilon = \mathbf{S} \cdot \tilde{\mathbf{u}} \tag{3.2}$$

Where $\mathbf{S}$ stands for the linear operator of the first derivatives that relates the strain with the displacements as the following equations show:

$$\epsilon = \mathbf{B}^e \cdot \mathbf{a}^e \tag{3.3}$$

$$\mathbf{B}^e = \mathbf{N}^e \cdot \mathbf{S} \tag{3.4}$$

Applying the Principle of the Virtual Work and minimizing the total potential energy, Eq. 3.5 is derived.

$$\mathbf{K}^e \cdot \mathbf{a}^e = \mathbf{r}^e - \mathbf{f}^e \tag{3.5}$$

Where $\mathbf{K}^e$ stands for the stiffness matrix of the element, $\mathbf{f}^e$ stands for the internal force set and $\mathbf{r}^e$ stands for the external force set of each element e.

The stiffness matrix can be obtained as shown in Eq. 3.6, where $\mathbf{D}$ stands for the material stiffness matrix.

$$\mathbf{K}^e = \int_v \mathbf{B}^T \mathbf{D} \mathbf{B} dV \tag{3.6}$$

The solution is obtained solving the system of equations defined in Eq. 3.7.

$$\mathbf{r}_i = \left(\sum_{e=1}^{m} \mathbf{K}_{i1}^e \right) \cdot \mathbf{a}_1 + \left(\sum_{e=1}^{m} \mathbf{K}_{i2}^e \right) \cdot \mathbf{a}_2 + \cdots + \sum_{e=1}^{m} \mathbf{f}_i^e \tag{3.7}$$

3.1.2 Hyperelasticity

Biological tissues are often considered as hyperelastic incompressible materials. These materials have a rubber-like behavior and they present a stress-strain relationship that is non-linear, isotropic and incompressible. In this research, it was assumed that the breast and the cornea present this type of behavior.

Given a solid subjected to a displacement field $u_i(x_k)$, each element of the deformation gradient tensor is defined as follows:

$$F_{ij} = \delta_{ij} + \frac{\partial u_i}{\partial x_j} \tag{3.8}$$

Where $\delta_{ij} = 1$ if $i = j$, and $\delta_{ij} = 0$ if $i \neq j$.

Having the strain energy density a function of the Left Cauchy-Green deformation tensor (Eq. 3.9) assures the isotropy of the constitutive equation.

$$\mathbf{B} = \mathbf{F} \cdot \mathbf{F}^{\mathbf{T}} \tag{3.9}$$

From the three eigenvalues of $\mathbf{B}$: e_1, e_2 and e_3, the principal

stretch directions are defined as follows:

$$\begin{aligned} \lambda_1 &= \sqrt{e_1} \\ \lambda_2 &= \sqrt{e_2} \\ \lambda_3 &= \sqrt{e_3} \end{aligned} \tag{3.10}$$

Considering **B** as the deformation measure, the stress-strain energy function $W(\mathbf{F})$ can be written based on the invariants of **B** (Eq. 3.11).

$$\begin{aligned} I_1 &= trace(\mathbf{B}) = \lambda_1^2 + \lambda_2^2 + \lambda_3^2 \\ I_2 &= \frac{1}{2}(I_1^2 - \mathbf{B}^2) = \lambda_1^2\lambda_2^2 + \lambda_2^2\lambda_3^2 + \lambda_3^2\lambda_1^2 \\ I_3 &= det(\mathbf{B}) = J^2 = det(\mathbf{F})^2 = \lambda_1^2\lambda_2^2\lambda_3^2 \\ J &= det(\mathbf{F}) \end{aligned} \tag{3.11}$$

$$W(\mathbf{F}) = \psi(I_1, I_2, I_3, J) \tag{3.12}$$

In this work, three different hyperelastic models were used: a neo-Hookean model, a Mooney-Rivlin model of second order, and an Ogden model.

Neo-Hookean model

The stress-strain function for the neo-Hookean model is defined by Eq. 3.13 [Treloar, 1948]. Where ψ stands for the strain

energy potential, I_1 stands for the first invariant, J stands for the determinant of the deformation gradient tensor, μ stands for the initial shear modulus of the material, and d stands for the material incompressibility parameter.

$$\psi = \frac{\mu}{2}(I_1 - 3) + \frac{1}{d}(J - 1)^2 \tag{3.13}$$

Mooney-Rivlin model

The constitutive equation of the Mooney-Rivlin model for second-order is given by Eq. 3.14 [Mooney, 1940; Rivlin, 1948]. Where C_1 and C_2 stand for the material elastic parameters, K_1 stands for the Bulk modulus, I_1 and I_2 stand for the first and second deviatoric strain invariants, and J stands for the determinant of the deformation gradient tensor.

$$\psi = C_1(I_1 - 3) + C_2(I_2 - 3) + \frac{K_1}{2}(J - 1)^2 \tag{3.14}$$

Ogden model

The definition of the energy potential function of the N-order Ogden model is given by Eq. 3.15 [Ogden, 1972]. Where N stands for the order, μ_i and α_i stand for the elastic parameters, λ_i stand for the three deviatoric stretches defined in Eq. 3.11, K_1 stands for the initial Bulk modulus, and J stands for the determinant of the elastic deformation gradient.

$$\psi = \sum_{i=1}^{N} \frac{\mu_i}{\alpha_i}(\lambda_1^{\alpha_i} + \lambda_2^{\alpha_i} + \lambda_3^{\alpha_i} - 3) + \frac{K_1}{2}(J-1)^2 \tag{3.15}$$

3.2 Optimization by genetic heuristics

The search of the elastic constants of the constitutive models proposed to characterize the mechanical behavior of the breast and the cornea was carried out by means of a parameter optimization algorithm driven by genetic heuristics.

Iterative search algorithms are often used to optimize a fit function $f(\mathbf{X})$ with an unknown shape by changing the input parameters $\mathbf{X}$ and using the output to minimize (or maximize) its value.

$$\hat{\mathbf{X}} = \arg\min f(\mathbf{X}) \quad \text{where } \mathbf{X} = \{x_1, x_2, \cdots, x_n\} \tag{3.16}$$

Since the fit function can present multiple minima, search algorithms such as gradient descent may get stuck in one of those minima thus being unable to provide the best solution. This problem can be avoided by running the algorithm multiple times with random initializations. Nevertheless, there are more effective approaches for the global optimization like meta-heuristics.

One of the most known meta-heuristics is the evolutionary computation [Fogel, 1995; Jong, 2006]. Inspired in biological evolution, this type of heuristic drives the search by using the candidate solutions to generate a new population iteratively. Evolutionary heuristics have been already used to characterize mass-spring

models successfully [Bianchi et al., 2004; Xu et al., 2009]. Genetic algorithms, a widely used meta-heuristic, was selected to drive the methodology to estimate the elastic parameters of the biomechanical models of the breast and cornea.

A Genetic Algorithm (GA) is a heuristic based on evolutionary computation used for optimizing problems [Chatterjee et al., 1996]. This heuristic allows the reduction of the computational cost of the parameter optimization since it focuses on the most promising areas while trying to explore the rest of the search space. A genetic algorithm handles a population of individual solutions (parents) to a given problem and drives the evolution of the subsequent steps of the search generating new candidate solutions (children). The population is modified by changing the individuals step by step, this evolution leads to the optimal solution of the problem. Genetic algorithms are prepared to work on complex optimization problems where the fit function can present multiple minima.

3.2.1 Genetic operators

In each iteration of the GA, a new set of candidate solutions is generated by three generation formulas:

- *Selection*: the best individuals (parents) are selected and used to breed the next population.
- *Crossover*: a combination of two parents forms a child.
- *Mutation*: parents are randomly modified to form a child.

The successive populations of the iterative search are created using these three genetic operators. Since only the best individuals are considered as parents, the average fit function value is equal or better in each iteration while the search interval becomes smaller, thus reducing the search space in each iteration.

The GAs control the proportion of children generated whether by selection, mutation or crossover with parameters which should be adjusted for each optimization problem in order to get the best results.

3.2.2 GA outline

The GA works following this outline:

1. *Initialize*: a random population of samples $\mathbf{X}_0$ is created. It is common to set an interval for each parameter to be found in order to help the algorithm to search in the area where the global minimum of the function may be located.

2. *New population generation*: iteratively, the algorithm creates a new candidate set of parameters $\mathbf{X}_i$ by means of the following steps:

   a) The algorithm computes the fit function $f(x)$ for each individual in the current set $\mathbf{X}_i$.

   b) Those individuals (called parents) with the best scores are selected.

   c) Parents with the best score are tagged as elite and pass

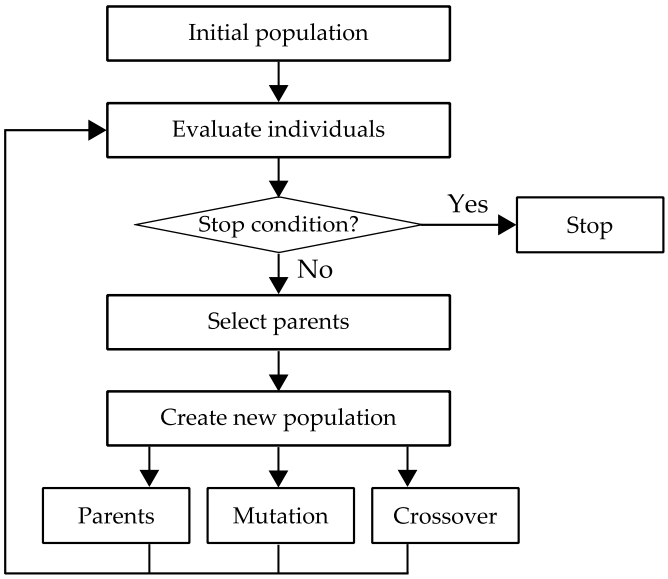

Figure 3.1: *Flowchart of the genetic algorithm*

directly to the next population.

d) Parents are used to generate new children both by mutation (randomly changing a parent) and by crossover (combination of several parents).

e) A candidate population $\mathbf{X}_{i+1}$ is created by joining elites and children.

3. *Termination*: step 2 is repeated until a stop condition is reached. This can be a specific number of generations, a timer, or when the function does not change within a tolerance range. The set of parameters that minimized the function will be designated as $\hat{\mathbf{X}}$.

A flowchart of the the genetic algorithm is shown in Figure 3.1.

3.3 Similarity coefficients

In Biomechanics there are several methods used to compare and/or validate the proposed biomechanical models in order to know their similarity regarding the real behavior of the organ. The work presented in [Crum et al., 2005] provides the accuracy of each registration method using the distance between fiducial landmarks attached to a real organ. On the other hand, the volume difference is also a measure that may provide information about the fit goodness of a biomechanical model and it was used in [Shi et al., 2008]. However, the comparison using fiducial landmarks entails comparing only specific points on the surface and does not consider the whole structure, ignoring the internal tissue distribution. The same problem has the volume difference which is not a valid measure since it is not able to distinguish situations in which the organ is in different positions or the volume do not change.

A similarity measure commonly used in medical imaging for validating biomechanical models is the Normalized Mutual Information (NMI) [Studholme et al., 1999]. Using this type of image-based comparison may result in inaccurate results since NMI does not consider the spatial distribution of the tissues but only the gray value entropy of both 3D images. In [Lee et al., 2010] a Fourier-based correlation technique was used to compare the accuracy of the deformed breast compression model. In this case, as the authors state, the technique only allows the comparison of images

from the same modality and it does not take into account any spatial information for the comparison.

In the recent literature, the similarity coefficients traditionally used in validation of segmentation techniques have started to be applied in the field of the computational biomechanics. Jaccard and Dice coefficients were used in [Balocco et al., 2010] to measure the goodness of a registration algorithm using the biomechanical properties in cerebral aneurysms and Hausdorff coefficient was used in [Vigneron et al., 2010] to validate a registration technique that uses a biomechanical model to simulate the deformation suffered by the brain immediately after opening the skull. Unfortunately, the use of only overlap-based coefficients (like Jaccard or Dice) does not provide information about the shape of the volume and using only distance-based coefficients (like Hausdorff) ignores the overlapped region.

The following section presents a study about how to apply similarity coefficients traditionally used for validation of segmentation techniques in order to assess the error committed between the simulation of the behavior of an organ and its real behavior.

3.3.1 Overlap and distance coefficients

The similarity coefficients usually operate over a 3D volume, thus abstracting all the processes from the number and type of elements of a mesh (tetrahedron, hexahedron...). In order to compare two finite element meshes, they must be first converted to a 3D volume, this process is called voxelization. Methods for validation of segmentations techniques are easily applicable to volume com-

parison and can provide different fit measurements depending on the error type that the coefficients measure. Both types of coefficients, based on volume overlap and based on distances were analyzed in order to know the combination that best measures the similarity of two 3D volumes. Two overlap-based coefficients and one distance-based coefficient were studied. Specifically Jaccard Coefficient, Dice Coefficient and Hausdorff Coefficient. These coefficients have provided the best results in volume comparison according to Cárdenes et al., 2009.

Jaccard Coefficient

Given two volumes X and Y, Jaccard Similarity Coefficient (JC) allows the comparison of the overlap between two data sets. JC is defined in Eq. 3.17. Its values go from 0 to 1, with 0 meaning no overlap and with 1 being a complete overlap.

$$JC = \frac{|X \cap Y|}{|X \cup Y|} \tag{3.17}$$

Dice Coefficient

Dice Coefficient (DC) [Dice, 1945] is very similar to Jaccard and it is defined in Eq. 3.18. Due to its equivalence with Jaccard, its values are defined in the same way, 0 meaning there is no overlap and 1 a complete overlap. This coefficient benefits more the overlapped elements and penalizes less the different ones than Jaccard.

$$DC = \frac{2|X \cap Y|}{|X|+|Y|} = \frac{2JC}{JC+1} \tag{3.18}$$

Hausdorff Coefficient

The Hausdorff Coefficient (H) was introduced by Hausdorff in 1962. This distance has been used in image comparison [Aspert et al., 2002; Lockett and Guenov, 2008; Vigneron et al., 2010] and its calculation has been improved to be applicable to big volumes [Huttenlocher et al., 1993].

Let's define the distance $d_V(i)$ as the distance of the voxel i to the closest voxel of a volume V. If $i \in V$, then $d_V(i)$ is zero. The comparison was performed between two volumes X and Y, corresponding to the simulation and real behavior of the tissue, respectively. For the calculation of d_X and d_Y, the euclidean distance transform (EDT) was used [Ragnemalm, 1993]. The EDT allows the obtainment of all the distances in a matrix. Hence, the extraction of any $d_V(i)$ is immediate.

The Hausdorff Coefficient (Eq. 3.19) uses this distance to provide a similarity value between two sets. It is defined as the maximum of the minimum distances between all the voxels of the volume X to all the voxels of the volume Y and viceversa.

$$H(X,Y) = \max_{\forall i}(d_X(i), d_Y(i)) \tag{3.19}$$

In order to perform a complete evaluation of the right fit between volumes, both overlap-based coefficients and distance-

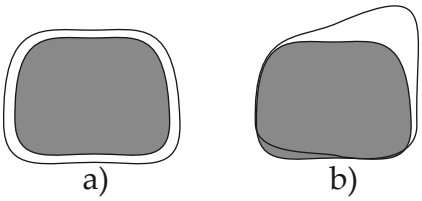

Figure 3.2: *Comparison of two different segmentations of an object a) and b), which provide similar value of the overlap-based coefficients.*

based coefficients must be considered together. Figure 3.2 shows an example in which JC or DC would provide a similar value for the comparison of both cases a) and b). Nevertheless, a) would be an admissible deformation and b) would not. Therefore, additional information can be used to distinguish these cases using, for instance, distance-based coefficients. Additionally, the same problem arises with distance-based coefficients, they may provide similar values in very different cases. As Figure 3.3 shows, the maximum distance present in both a) and b) is the same and the Hausdorff coefficient would provide similar values. Therefore, it could be difficult to differentiate these deformations without using, for instance, overlap-based coefficients.

3.3.2 Analyzing the performance of the coefficients

The purpose of this study was to know which are the most discriminant coefficients to compare the similarity of two volumes [Lago et al., 2012a]. In the case of the overlap-based coefficients, Jaccard and Dice coefficients were analyzed. Regarding the distance-based coefficients, twenty four modifications of the Hausdorff Coefficient were studied in order to create a large set of measures to be studied. The 24 modifications corresponded to the

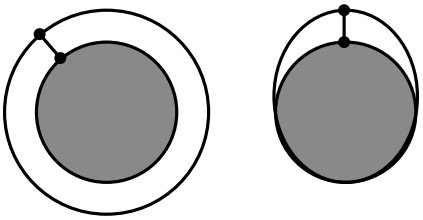

Figure 3.3: *Comparison of two different segmentations of an object a) and b), which provide similar value of the original Hausdorff coefficient.*

coefficients presented in [Dubuisson and Jain, 1994] and defined with the direct distances shown in Eq. 3.20 to 3.25.

$$d_1(X,Y) = \min_{x \in X}(d_Y(x)) \tag{3.20}$$

$$d_2(X,Y) = K^{50th}_{x \in X} d_Y(x) \tag{3.21}$$

$$d_3(X,Y) = K^{75th}_{x \in X} d_Y(x) \tag{3.22}$$

$$d_4(X,Y) = K^{90th}_{x \in X} d_Y(x) \tag{3.23}$$

$$d_5(X,Y) = \max_{x \in X}(d_Y(x)) \tag{3.24}$$

$$d_6(X,Y) = \frac{1}{N_X} \sum_{x \in X} d_Y(x) \tag{3.25}$$

Where $K^{Pth}_{x \in X}$ represents the Pth percentile of all the sorted distances and N_X stands for the number of elements of the set X. Combining these distances with the combinations shown in Eq. 3.26 to Eq. 3.29, the whole set of modified Hausdorff metrics is

constructed.

$$f_1(X,Y) = \min\left(d_i(X,Y), d_i(Y,X)\right) \tag{3.26}$$

$$f_2(X,Y) = \max\left(d_i(X,Y), d_i(Y,X)\right) \tag{3.27}$$

$$f_3(X,Y) = \frac{d_i(X,Y) + d_i(Y,X)}{2} \tag{3.28}$$

$$f_4(X,Y) = \frac{N_X d_i(X,Y) + N_Y d_i(Y,X)}{N_X + N_Y} \tag{3.29}$$

	f_1	f_2	f_3	f_4
d_1	D_1	D_2	D_3	D_4
d_2	D_5	D_6	D_7	D_8
d_3	D_9	D_{10}	D_{11}	D_{12}
d_4	D_{13}	D_{14}	D_{15}	D_{16}
d_5	D_{17}	D_{18}	D_{19}	D_{20}
d_6	D_{21}	D_{22}	D_{23}	D_{24}

Table 3.1: *The 24 modified Hausdorff distances*

Therefore, the direct distances d_i are combined with the f_j equations obtaining a set of 24 modified Hausdorff Coefficients (Table 3.1). It is noticeable that D_{18} corresponds to the original Hausdorff distance defined in Eq. 3.19. The distances from D_1 to D_4 were discarded because of their constant value throughout the problem domain, thus leaving 20 Hausdorff modifications.

In addition to the modifications of the Hausdorff distance and, by taking advantage of the distance calculation, the distance of the surface voxels of a volume X to the nearest voxel of a volume Y (and viceversa) were taken into account. The average of

these distances (corresponding to $d_6(X, Y)$ and $d_6(Y, X)$) and their standard deviations were also used for the analysis of the volume comparison. These values are indicators of the homogeneity of the distances between the surfaces of the volumes. Additionally, the signed mean (Eq. 3.30) was added to the set of coefficients to be studied since it could indicate the deviation of one volume with regard to the other one and viceversa.

$$SM = d_6(X, Y) - d_6(Y, X) \tag{3.30}$$

Experimental set-up

Let's summarize the 28 coefficients that were analyzed to select the best set to compare a simulated deformation of an organ to the real one: two coefficients based on overlap (Jaccard and Dice coefficients), the widely used volume difference ($\mathbf{\Delta}V$), the 20 modified Hausdorff coefficients (D_5 to D_{24}), the signed mean (SM), and the means and standard deviations of the distances between both volumes ($mean_{d_X}, mean_{d_Y}, std_{d_X}, std_{d_Y}$).

The experiment designed for the selection of the best metrics was a cantilevered bar (Figure 3.4) on which a force F_0 was applied to construct the gold standard deformation. A comparison between the gold deformation caused by F_0 and other 8 different deformations (referred to as incorrect deformations) was performed. The 8 configurations combine forces in different directions and intensities as follows ($F_1 = F_2 = F_3 = F_4 = 120\%F_0$):

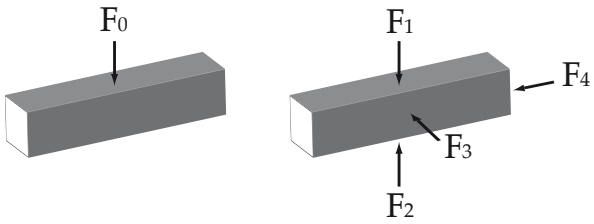

Figure 3.4: *Experiment of the bar and the forces applied.*

- Def_1: 110%F_0 is applied
- Def_2: F_1 is applied
- Def_3: F_1 and F_4 are applied
- Def_4: F_1 and F_3 are applied
- Def_5: F_2 is applied
- Def_6: F_3 is applied
- Def_7: F_4 is applied
- Def_8: F_3 and F_2 are applied

Results

To select the best coefficients, the comparisons of the 8 configurations with the gold standard were performed thus obtaining 28 curves for the corresponding coefficients. The goal was to select the most significant metrics of the set, those which better discriminated the worst configurations from the best ones. The values of

the coefficients obtained in the comparison of these simulations are shown in Figure 3.5. It can be considered the deformations from best to worst (1 to 8). The values were normalized to be easily compared and divided in six plots to allow for a better legibility.

From all the modifications of the Hausdorff coefficient, those whose Def_5, Def_6, and Def_7 configurations did not show the worst values were rejected since these deformations must be considered the least similar to the gold deformation. The remaining Hausdorff modifications were still valid. However, the D_{22} Hausdorff modification, named as modified Hausdorff distance (MHD), was selected since, according to [Dubuisson and Jain, 1994], its values increase monotonically with the amount of difference, and is better at evaluating volume matching than the other distances thus having more discriminatory power. Furthermore, it can be considered that, in this experiment, neither the volume increment nor the signed mean were useful to differentiate a good adjustment from a bad one, therefore they were rejected.

Regarding overlap-based coefficients, both Jaccard and Dice showed a similar behavior. Therefore, a different experiment for the selection of the best overlap-based coefficient to perform volume comparisons was performed. A cylinder was compared with another one, of the same size and shape, but rotated on its own axis. The union of both volumes with two different rotations is shown in Figure 3.6.

The values obtained in this experiment are shown in Figure 3.7. Jaccard and Dice coefficients represented the level of overlapping between the two cylinders, giving the lowest value at the middle

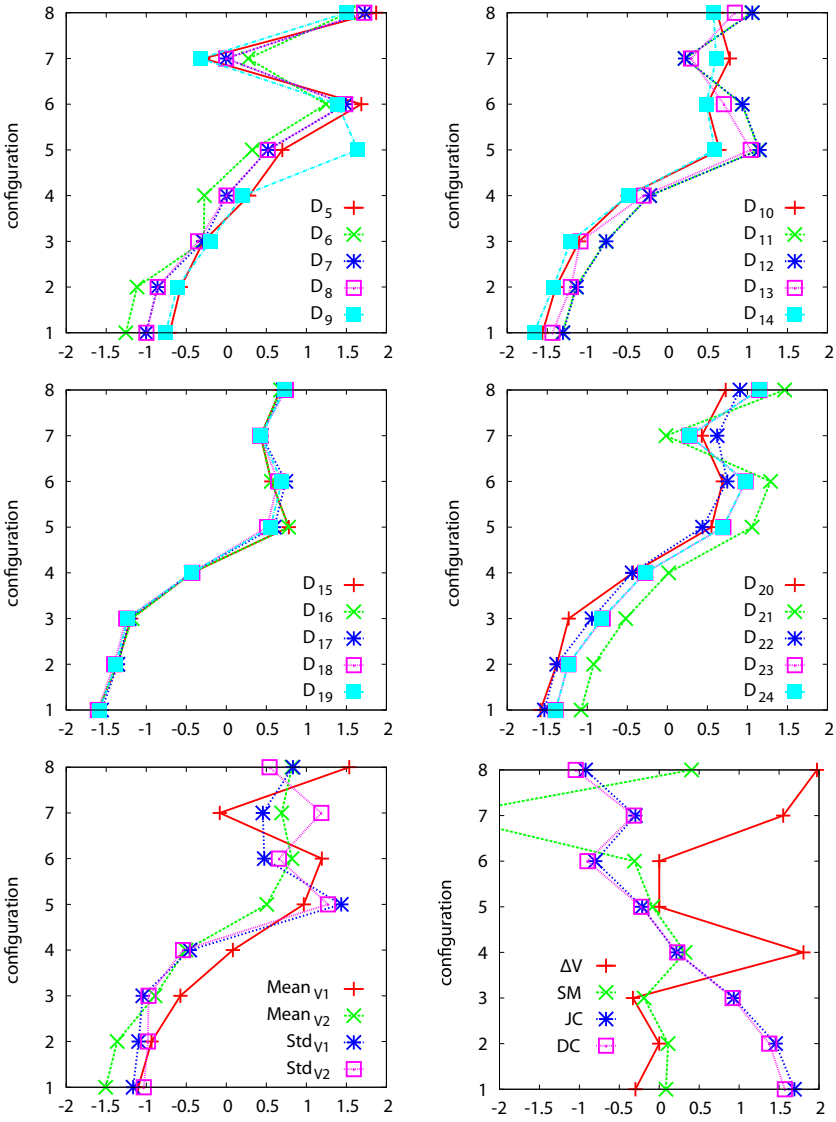

Figure 3.5: *Values of all the metrics for the 8 configurations of the bar.*

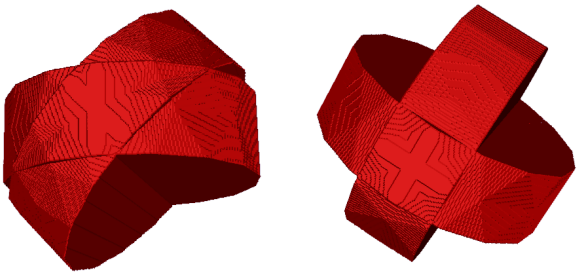

Figure 3.6: *Volume comparison of a rotated cylinder with respect to another.*

of the curve (90°). This curve also shows how Dice discriminated less than Jaccard because of the lower decay of the Dice coefficient curve compared with the decay of Jaccard coefficient one. Therefore, Jaccard was selected as the best overlap-based coefficient to take into account.

3.3.3 Geometric Similarity Function

The previous study showed that Jaccard coefficient (JC) and the modified Hausdorff distance (MHD) were suitable coefficients to compare the simulated deformation of an organ to the real one since they provide more information about the fit than the classic comparison methods as volume difference or positions of markers. They show how the error (or the lack of it) is distributed throughout all the volume and provide information about the shape difference. However, as it was stated before, using only an overlap-based measure or a distance-based coefficient does not provide enough information to know whether two volumes are similar or not. Therefore, it is necessary a combination of both

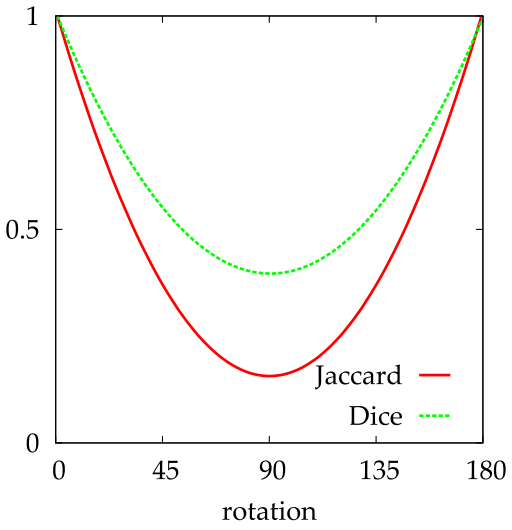

Figure 3.7: *Jaccard and Dice values of the comparison of a rotated cylinder with respect to another, from 0° to 180°.*

types of coefficients.

For that purpose, our group proposed a new coefficient called GSF (Geometric Similarity Function) defined in Eq. 3.31 [Martínez-Martínez et al., 2012, 2013b]. The higher similarity between two volumes, the lower value of the GSF, being -∞ when the volumes are identical. The GSF units are not easily interpretable since the function is a logarithm of a distance weighted over the overlap. Therefore, it was only used as a fit function for the genetic heuristic and the results of the following chapters only show the values of JC and MHD.

$$GSF = \log\Big((1 - JC) \times MHD\Big) \tag{3.31}$$

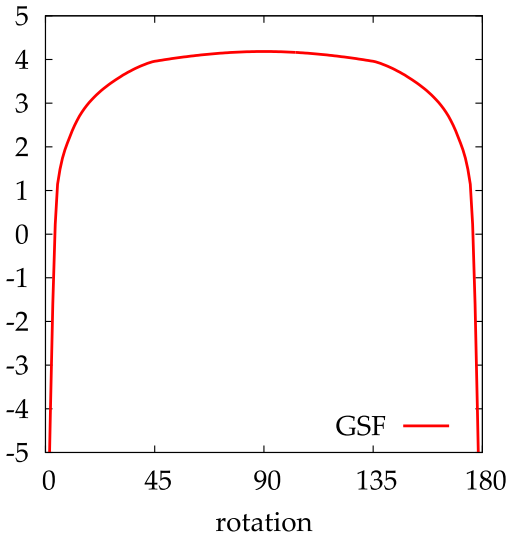

Figure 3.8: *GSF values of the comparison of a rotated cylinder with respect to another, from 0°to 180°.*

The use of both parameters in the Geometric Similarity Function combines the benefits of the overlap and the distance measure. It should be emphasized that, these coefficients can be used in combination with traditional biomechanical information as, for example, strain-stress curves, or force-displacement curves, if they were available.

Figure 3.8 shows the GSF values for the same rotating cylinder from the previous experiment. It is noticeable the high decay of the values when the similarity of the cylinders increases (angle near 0 and near 180). This is a great indicator of the high sensitivity of the GSF with regard to small differences between volumes. For this reason, the GSF is appropriate for the validation of biomechanical models and as a fit function for the genetic algorithm.

3.4 Conclusions

This chapter has detailed the materials and methods used to develop the methodology reported in this thesis. The theoretical base of the biomechanical models that were used to characterize the behavior of the organs was established, focusing on the selected hyperelastic models that model the biomechanical behavior of the breast and the cornea tissues.

Genetic heuristics have also been presented as the basis of the iterative search algorithm implemented to estimate the elastic constants of the models in complex domains.

Finally, a study to select which coefficients are the best to compare two volumes has also been reported. These coefficients allowed the definition of the fit function to be used by the genetic heuristic. This function, the Geometric Similarity Function, considers the information of two types of similarity coefficients: an overlap-based (Jaccard coefficient) and a distance-based (modified Hausdorff distance), and is the core of the iterative search of parameters.

Chapter 4

Characterization of the biomechanical behavior of the breast

As mentioned in previous chapters, the accuracy of a patient-specific biomechanical model of the breast is a major concern for applications such as surgical simulation, surgical guidance or cancer diagnosis. However, the elastic constants that define the biomechanical behavior of the breast tissues are highly variable among patients and their estimation becomes a very difficult task.

This chapter describes a methodology based on the simulation of the mammographic compression during an MRI-guided biopsy for the *in-vivo* characterization of the biomechanical behavior of the breast. An iterative search algorithm is used to find the elastic

constants of the constitutive equations of the model proposed to characterize the three main tissues of the breast: fat, glandular tissue and skin. The methodology was applied for the characterization of breast software phantoms [Pokrajac et al., 2012]. The biomechanical model chosen to characterize the breast tissues was the anisotropic neo-Hookean hyperelastic model proposed by Han et al., 2012. Results from this analysis showed that following the proposed methodology, the elastic properties of each tissue were estimated with a mean relative error of about 10% [Lago et al., 2014a].

4.1 Breast anatomy

The female breast is a glandular organ formed by different internal structures, namely: adipose tissue, fibroglandular tissue, Cooper's ligaments, the ductal network and, finally, a complex mixture of smaller structures like blood vessels, nerves and lymphatics.

The fibroglandular tissue region has a conical form extending from the nipple to the chest wall. This cone is called the parenchymal cone and it is surrounded by adipose tissue which allows the mobility on the chest wall [Egan, 1988]. The adipose tissue region is formed by different adipose compartments separated by the Cooper's ligaments. Those suspensory ligaments are fibrous structures connected to the skin that provides structural support to the breast. The ductal network is formed by ducts starting in the glandular secretory lobes (or gland lobules) and ending in the nipple, the ducts are surrounded by glandular tissue. An average

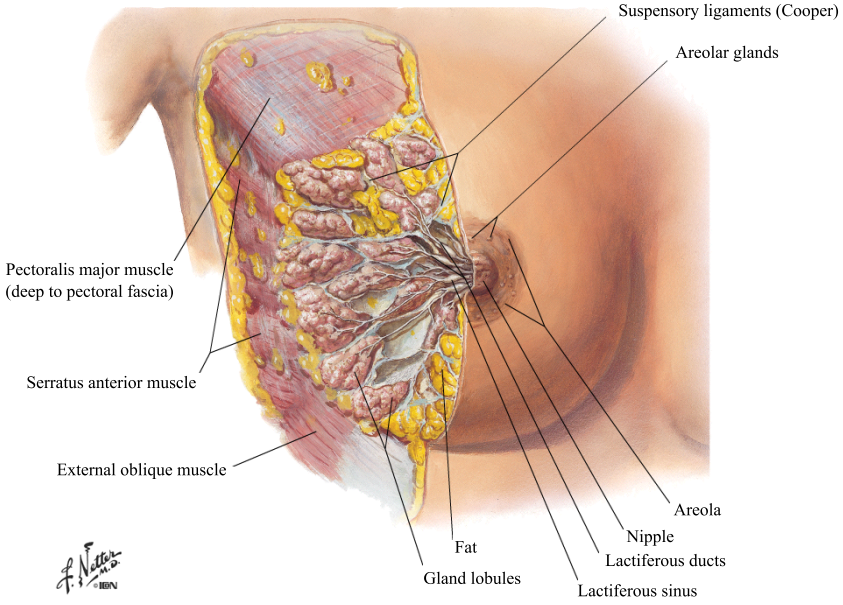

Figure 4.1: *Mammary gland (anterolateral dissection) [Netter, 1989]*

adult breast contains 15-20 lobes each one of them has its own major duct [Lamarque, 1984]. The breast is attached to the pectoral muscle, which connects it to the chest wall between the 2nd and the 6th ribs. The breast is wrapped by the skin, a combination of cutaneous and subcutaneous layers with a thickness between 0.5 mm and 3 mm [Ulger et al., 2003; Gefen and Dilmoney, 2007]. Figures 4.1 and 4.2 show a section of the female breast in anterolateral an sagittal directions respectively [Netter, 1989].

4.2 Breast imaging systems

Early detection of cancer is of great importance since an early treatment may be crucial for the patient. X-ray mammography is

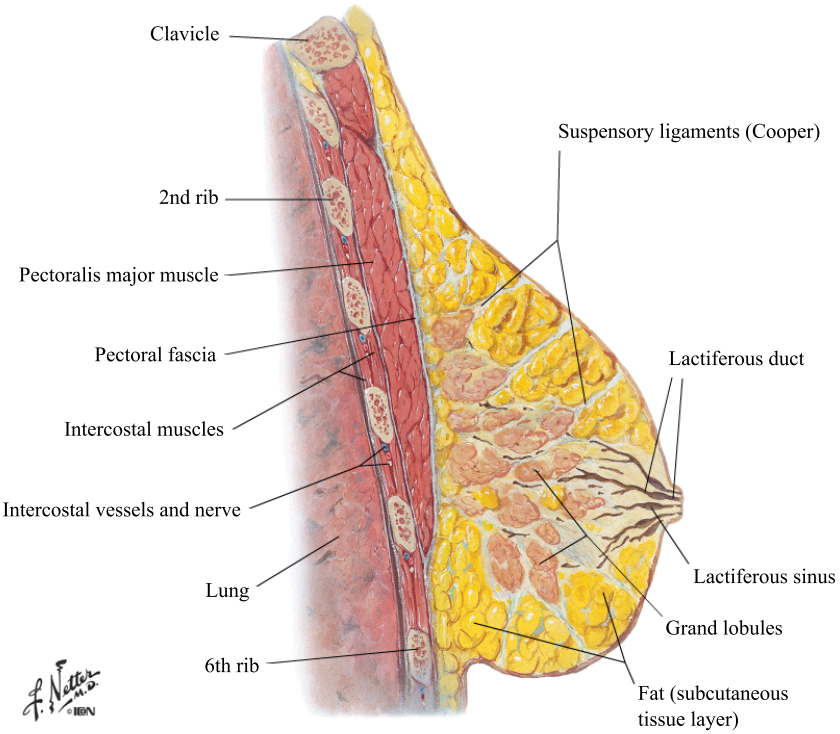

Figure 4.2: *Mammary gland (sagittal section) [Netter, 1989]*

the most common imaging modality for breast cancer diagnosis [Schulz-Wendtland et al., 2009] but there are some other common exploration techniques such as magnetic resonance images (MRI) or tomosynthesis.

4.2.1 X-ray Mammography

X-rays were discovered in 1895 by Wilhem Conrad Roentgen thus being the oldest non-invasive technique of body imaging. An X-ray is an electro-magnetic radiation that is able to traverse the human body. The thickness and density of human tissues affect the magnitude of absorption of X-rays introducing a difference in the X-ray beam past the patient that is captured by a detector. The denser the tissue, the more X-rays it absorbs [Johns and Yaffe, 1987].

The generation of the X-rays is performed by accelerating an electron beam in a vacuum tube directing it towards the anode. The deceleration of the electrons produces electromagnetic energy (X-ray photons) which traverses the material in their path. In digital mammography, the X-rays fall upon a special detector which transforms the X-rays into electrical signals. These signals are used to produce images of the breast and sent to a computer for further processing.

The absorption of the X-rays causes the ionization of the traversed tissues thus needing a strict control of the dose received by the patient. For that purpose, a filter is placed between the generator and the patient in order to control the power of the X-ray. Specifically, for mammography imaging the X-ray energy needed

is low [Curry et al., 1990]. However, the area around the nipple may be overexposed to the X-rays while the region nearest to the chest wall may be underexposed causing a low-quality image. To avoid this problem, the breast is placed between two plates that compress it up to a 50% of its original size thus balancing the thickness of the breast in the X-ray direction as well as spreading the tissues in a larger surface reducing the possible overlap of interesting regions. The amount of compression is not a fixed value and it may vary between patients and acquiring sessions. There are two typical compression types: cranio-caudal (CC) compression, in which the plates are placed horizontally, and mediolateral oblique (MLO) compression, in which the plates are rotated up to 70°. Figure 4.3 shows the mammography device and an example of both MLO and CC mammograms of the same breast.

4.2.2 Magnetic Resonance

In magnetic resonance (MR) devices, a magnetic field is applied on the breast thus changing the magnetic equilibrium of the tissues and then, a radiofrequency pulse disturbs the magnetization. The tissues are bound to recover their initial magnetism thus emiting electromagnetic waves towards an antenna that detects this variation and generates a 2D image [Hesselink, 2006]. This type of wave is completely innocuous for the patient and it is able to traverse the bones without energy loss. This process is repeated in several 2D slices and the result is a 3D image of the studied region.

Breast MRI is usually performed in different configurations which can attenuate certain tissues. Both T1 configuration (fat sup-

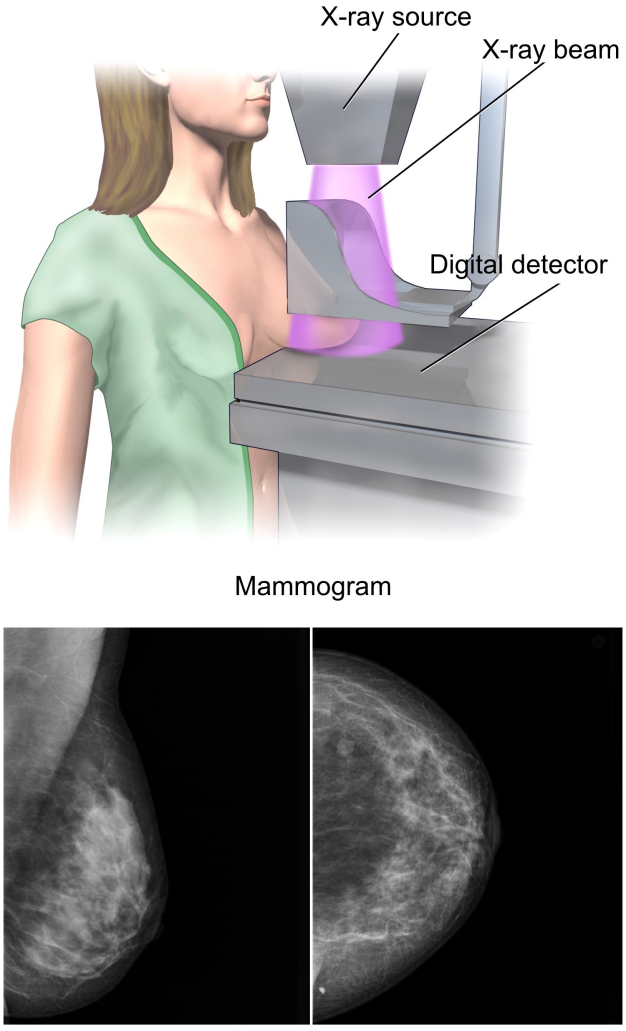

Figure 4.3: *Top: Mammography device used in CC position. Bottom Left: MLO X-ray mammogram. Bottom Right: CC X-ray mammogram*

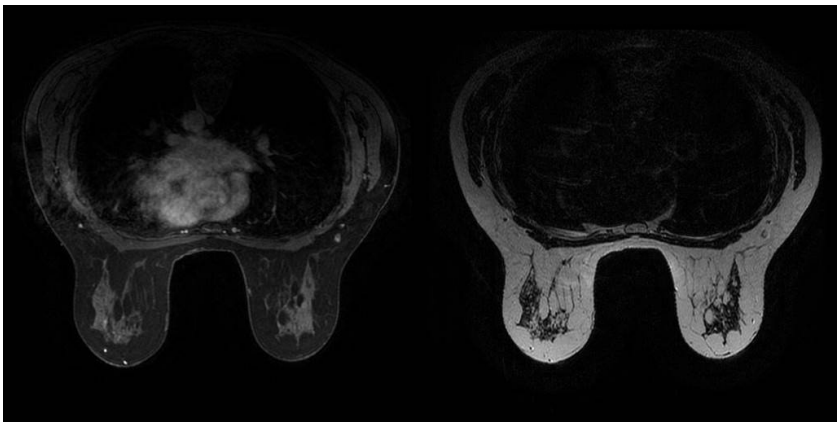

Figure 4.4: *MRI slice of the chest in two different configurations T1 (left) and T2 (right)*

pression) and T2 configuration of a breast MR image are shown in Figure 4.4. This modality is less common than X-ray mammography and it is used as an alternative imaging technique when there are suspicious areas that are not successfully distinguished in the X-ray mammography.

The MRI can also be used for breast guided biopsy. This is useful when the lesion cannot be detected in the X-ray mammography or by ultrasound. The patient lays in prone position in the MRI scanner as Figure 4.5 shows. The breast is placed between two plates which compress it to avoid displacements that can cause maladjustments during the biopsy. The scanner takes MR images in between the moments when the clinician operates with a needle, trying to reach the lesion. The procedure ends when a sample of the lesion is retrieved and a little marker is placed in the biopsy site. This marker is used to localize the lesion afterwards for future treatments.

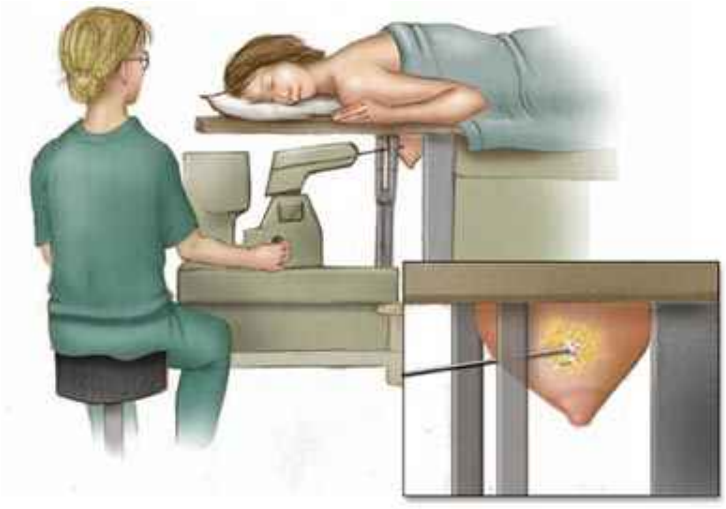

Figure 4.5: *MRI biopsy device. © Mayo Foundation for Medical Education and Research.*

4.3 Software breast phantoms

Virtual clinical trials (VCTs) whose images can be generated using software phantoms represent an important pre-clinical alternative for validating imaging systems in different modalities. Software phantoms can be used to create large data-sets of synthetic images with known ground truth about the simulated anatomy. They also offer flexibility to cover anatomical variations in the shape, size, and tissue distribution [Bakic et al., 2002].

Breast software phantoms, in particular, allow the creation of large sets of samples to simulate the images provided by the different types of imaging systems commonly used in breast cancer diagnosis: X-ray mammography, magnetic resonance (MR), or computerized tomography (CT) [Bakic et al., 2011]. Software

phantoms can be applied to know the feasibility of a wide range of studies as: simulation of multimodality imaging systems [Diekmann et al., 2009; Bakic et al., 2011; Chen et al., 2011; Chui et al., 2012], evaluation of breast dosimetry [Dance et al., 2005; Zhou et al., 2006; Ma et al., 2009; Sechopoulos et al., 2012], or evaluation of registration techniques [Richard et al., 2006].

Realistic virtual breast phantom development has been studied since early 2000's. Early development of 3D virtual breast phantoms was presented by [Bliznakova et al., 2003, 2010]. This phantom uses a combination of 3D geometrical primitives and voxel matrices including not only the Cooper's ligaments, skin and pectoral muscle but also the duct system and lobular units (Figure 4.6). This method generates a phantom which consists in a 3D mammographic texture, combination of all the primitive geometries in a voxelized 3D space. However, this type of phantom is only useful for mammographic simulations and simulation of X-ray modalities.

Similarly, the phantom developed by [Chen et al., 2011] also has the ability for multimodality imaging simulation. In this case, the phantom is formed by a random generation of skin, fat tissue, glandular tissue and a network of ductal trees. A compression model is applied and the compressed phantom is used to simulate image modalities such as mammography, computer tomography or tomosynthesis.

In [Li et al., 2009], the breast phantom is generated by means of real breasts. The segmented data from a real breast CT is used to create a model for the breast which is later compressed to sim-

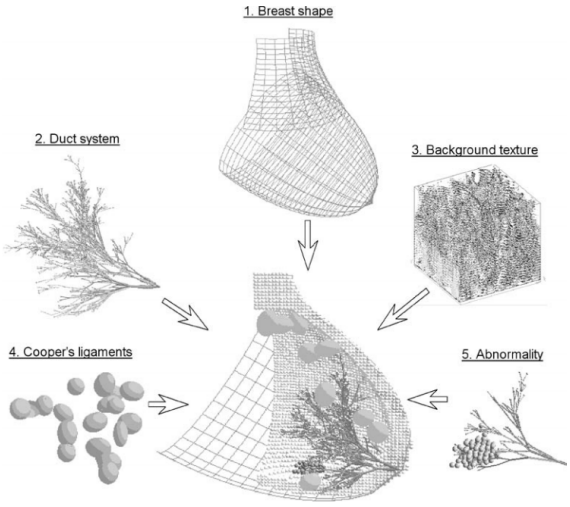

Figure 4.6: *Phantom by Bliznakova et al.*

ulate the mammography positioning (Figure 4.7). However, its dependence on a real breast reduces its variability since it is tied to the number of samples thus reducing the automaticity.

Recently, the work by [Bhatti and Sridhar-Keralapura, 2012] presented a complex 3D virtual breast phantom aimed to investigate the biomechanics of the elastography (Figure 4.8). This phan-

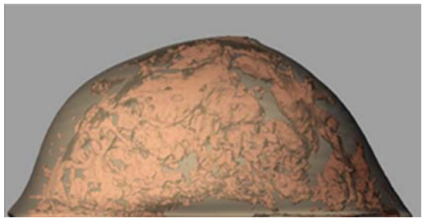

Figure 4.7: *Phantom by Li et al.*

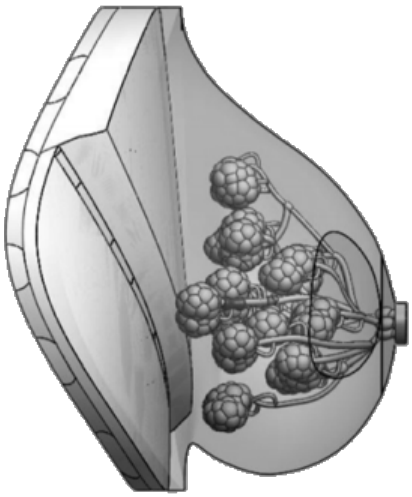

Figure 4.8: *Phantom by Bhatti and Sridhar-Keralapura*

tom is created by a mechanical design tool and can be parametrized in tumor location, glandular density and ductal structure. Although being very realistic, this phantom needs a manual process to generate most of the geometry and it was not tested for large deformations like mammographic compression.

The work by Bakic et al., 2002 presented a methodology for generating a computer breast model with realistic internal tissue distribution, including fat tissue, glandular tissue, Cooper's ligaments, and skin (Figure 4.9). These phantoms have been used in various clinical breast imaging modalities including digital mammography and digital breast tomosynthesis [Bakic et al., 2010; Vieira et al., 2013; Young et al., 2013], ultrasound tomography [Yang et al., 2012], and magnetic resonance [Nishikawa et al., 2011]. Later, they improved the model by using a region growing

Figure 4.9: *Phantom by Bakic et al., 2011*

algorithm thus accelerating the generation process and enhancing the realism of the internal tissue distribution [Bakic et al., 2011]. Finally, the phantom generation was also accelerated on the Graphical Processing Unit (GPU) using octrees [Pokrajac et al., 2012; Chui et al., 2012]. This is the phantom that was used to prove the methodology due to the ability of the algorithm to generate phantoms controlling the shape, size and fat/glandular ratio easily. An example of this phantom is shown in Figure 4.10.

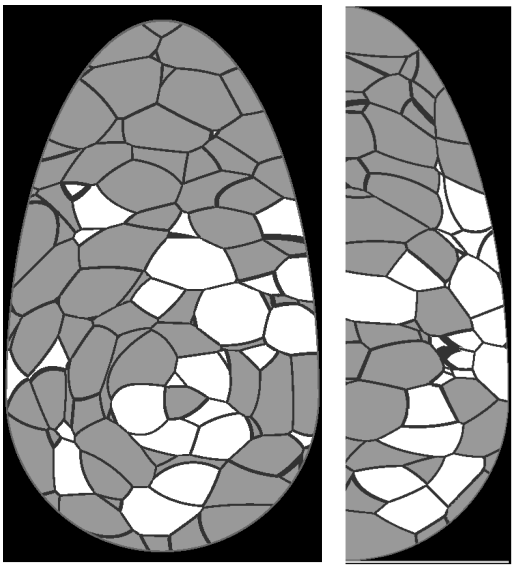

Figure 4.10: *Left: coronal section of a raw phantom. Right: mediolateral section of the corresponding phantom. Each gray level denotes each tissue type: white pixels correspond to the glandular tissue, light gray pixels correspond to the fat tissue, dark gray lines correspond to the Cooper's ligaments and mid-dark gray pixels surrounding the phantom correspond to the skin. [Pokrajac et al., 2012]*

4.4 Study of the mesh quality

This study was motivated by the necessity of generating large data-sets of synthetic X-ray mammograms for virtual clinical trials.

In order to get an accurate solution for the simulation of the compression of the breast, the finite element method (FEM) arises as the best method to predict the breast tissue distribution after mammographic compression [Matthews and West, 1972; Rajagopal et al., 2006; Han et al., 2011; Lago et al., 2012b,c, 2013a].

However, the iterative nature of this method is usually slow and becomes a bottleneck in the pipeline of generation of virtual breast images if adequate meshes are not used in the process. The simulation of the mammographic compression is the slowest step and the quality of the finite element mesh constructed to perform that simulation is of great importance for the accuracy and efficiency of this pipeline [Lago et al., 2013b].

Mesh quality should be an important issue to consider when dealing with realistic simulations of the biomechanical behavior of the soft living tissues. Generation of FE meshes that accurately represent the geometry of organs as the breast is a well-known problem in soft tissue biomechanics. The quality of the FE meshes constructed for these organs can affect the solution of simulations carried out using the FEM since low quality meshes may lead to unrealistic results or may present convergence problems. However, many works do not perform mesh quality analysis before the FE simulations [Bucki et al., 2011; Burkhart et al., 2013].

Patient-specific FE meshes that consider the different tissues of the breast can be automatically generated by commercial software packages. However, these meshing software usually create irregular meshes due to the complexity of the breast internal tissues [Tanner et al., 2006a; Kellner et al., 2007]. Automatic generation of patient-based finite element meshes considering the different tissues of the breast usually lead to bad quality elements (tetrahedra in this case), especially at the boundaries between the different tissues. These regions are usually meshed with many elements, often irregular or distorted, in order to fit the boundary surfaces. A manual intervention for refining these regions is needed in or-

der to improve the mesh quality, for avoiding non-convergences, and for reducing the computational cost of the FEM [Bucki et al., 2011]. Being able to use regular meshes with good-quality elements may reduce the time consumed by the FEM and the risk of non-convergence.

In this section, a comparison of the breast tissue distribution after the simulation of the compression of an X-ray mammography by two different meshing approaches was detailed. A mesh created with elements adapted to the distribution of the internal tissues (*adaptive mesh*) and a mesh constructed with regular elements (*homogeneous mesh*) automatically generated by a commercial software were used for this study.

4.4.1 Materials and Methods

Synthetic generation of X-ray mammograms involves performing three major tasks: generating a 3D software phantom, simulating the mammographic compression, and projecting the deformed phantom to obtain a 2D virtual mammogram. The generation of the 3D breast anatomy of the phantom was carried out using the computer anthropomorphic breast phantoms developed at the University of Pennsylvania (UPenn) described in Section 4.3 [Bakic et al., 2002, 2011; Pokrajac et al., 2012].

Generation of the finite element mesh

Once the software phantom was generated, the next step was to obtain the finite element mesh from the virtual geometry. For that, two approaches were considered:

- *Adaptive mesh*: constructing the mesh considering the different tissues of the breast.
- *Homogeneous mesh*: constructing the mesh considering the whole breast as a single tissue and assigning material properties to the elements afterward.

In the first case, the meshing software draws the boundaries between tissues creating small elements on those regions and bigger elements on the areas with the same material. The result is a large number of poor quality elements dedicated to draw the boundaries.

In the second case, the meshing software is blind to the breast tissues, thus creating a regular mesh of the whole breast as if it was only made out of a single material. In this case, the meshing algorithm is able to create elements with more regular shape and size since it finds no restrictions due to the internal tissue distribution. Regarding how this algorithm takes into account the tissue distribution, the most prevalent material in an element is assigned to it afterward.

In both cases, the commercial software Simpleware® was used to create meshes using tetrahedral elements. The skin and Cooper's ligaments were not meshed separately since these structures are not clearly visible in some clinical modalities [Solves Llorens et al., 2012; Han et al., 2012]. Moreover, narrow structures like the skin would require a large number of irregular elements in the adaptive meshing. Therefore, for this study, the breast was assumed to be formed by fat tissue, which included skin and

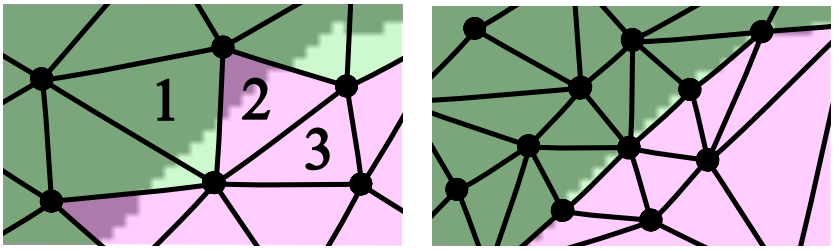

Figure 4.11: *Material distribution between elements in homogeneous mesh (left) and adaptive mesh (right). Dark material is assigned to Triangle #1 while clear material is assigned to Triangles #2 and #3. The example is in 2D for visualization purposes.*

Cooper's ligaments; and glandular tissue. The adaptive meshes were obtained directly by meshing these two materials, while the homogeneous meshes needed a further processing since they were meshed without considering the internal tissue distribution. For these meshes, the gray values of the phantom at the vertices and centroid were extracted for each tetrahedron and the assigned material was chosen as the most prevalent material from these 5 points (Figure 4.11).

The quality of the tetrahedra of a mesh can be measured by five different coefficients defined as equations from 4.1 to 4.5 show [Joe, 1991; Field, 2000; Edelsbrunner, 2001; Persson and Strang, 2004], where for tetrahedron t, R_t stands for its radius, E_t stands for the length of its edges, S_t stands for its solid angle, and V_t stands for its volume. All coefficients are in the range $[0-1]$ representing 0 the worst quality and 1 the best quality.

$$M_1 = 3 \times \frac{R_t^{insphere}}{R_t^{circumsphere}} \tag{4.1}$$

$$M_2 = 2\sqrt{6} \times \frac{R_t^{insphere}}{\max E_t} \tag{4.2}$$

$$M_3 = 12 \times \frac{(3 \times V_t)^{2/3}}{\sum_1^6 E_t^2} \tag{4.3}$$

$$M_4 = \min S_t \tag{4.4}$$

$$M_5 = \frac{\min V_t}{\max V_t} \tag{4.5}$$

On the other hand, widely used FE software packages like ABAQUS® or ANSYS® usually perform a quality test on the finite element mesh. These software packages show messages of warning when the aspect ratio of a tetrahedron is not good enough. The aspect ratio of a tetrahedron is defined as the ratio between the longest edge and the shortest normal from one vertex to the opposite face and it is related to the angles between faces. A regular tetrahedron (Figure 4.12, left) has an aspect ratio of 1.

All these coefficients were taken into account to measure the quality of the constructed meshes.

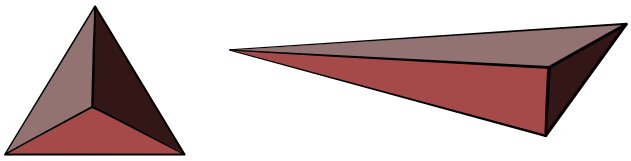

Figure 4.12: *Regular tetrahedron with a high aspect ratio (left) and another one with lower aspect ratio (right).*

Table 4.1: *Parameters used for the neo-Hookean model.*

	μ	ν
fat	12 750 Pa	0.49
glandular	36 750 Pa	0.49

4.4.2 Simulation of the mammographic compression

To perform this study, the neo-Hookean hyperelastic model described in Section 3.1.2 was chosen to simulate the deformation of the breast tissues in the compression during X-ray mammography. The parameters used for this model were taken from the literature [Gefen and Dilmoney, 2007] and are shown in Table 4.1.

The mesh of the breast phantom was placed between two rigid plates (Figure 4.13) and, as boundary conditions, the nodes belonging to the chest wall were restricted in the chest wall-nipple direction. Additionally, the nodes already in contact with the fixed plate were restricted in all directions in order to avoid rigid body motion [Ruiter et al., 2006]. A sliding contact interaction without friction was defined between the breast surface and both plates in order to facilitate the FE simulation. The reason was that the friction coefficient between the breast and the plates is unknown [Shih et al., 2010]. Finally, a displacement was applied to the mobile plate in order to compress the breast up to 50% of its thickness

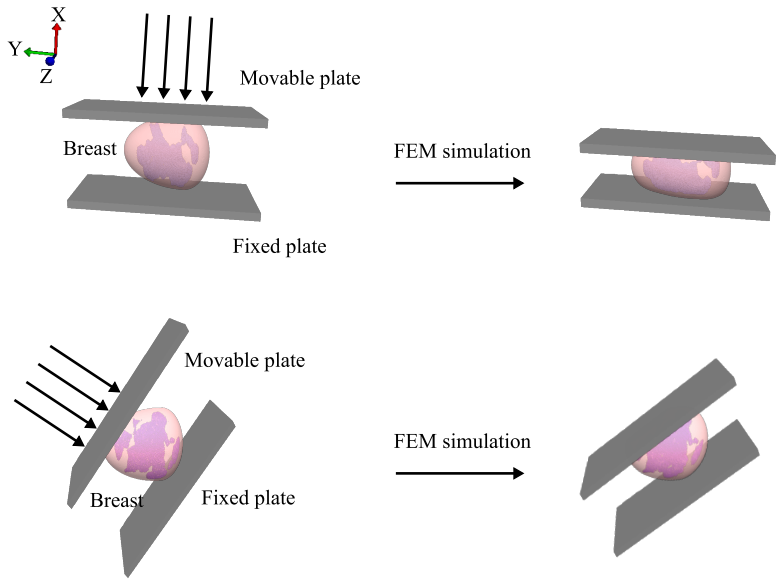

Figure 4.13: *Finite element model of a phantom before and after the mammographic compression in CC direction (top row) and MLO direction (bottom row).*

in Craneo-Caudal direction (CC) and up to 25% in Medio-Lateral Oblique direction (MLO). Like in a real X-ray mammography, the plates were placed horizontally for the CC compression while for the MLO compression the plates were rotated 45°.

Similarity coefficients

In order to compare the performance of the homogeneous mesh with regards to the adaptive mesh, the Jaccard Coefficient and the Modified Hausdorff Distance presented in Section 3.3 were

considered. Additionally, centroid distance and volume difference were also computed since they provide a very intuitive value of the similarity between two compartments.

Generation of the compressed 3D phantom

Once the breast mesh was compressed, the deformed 3D phantom was obtained. The compressed phantom is the result of interpolating the original 3D phantom as a texture. Each tetrahedron (before and after the deformation) was used to know how the original phantom had to be deformed. The interior gray values of each tetrahedron before the deformation were interpolated to obtain the new position in the deformed tetrahedron, thus creating the new 3D texture. This step was run on the GPU in order to accelerate the generation.

4.4.3 Results of the mesh quality analysis

Ten phantoms of ratio dense/fat tissue between 7% and 35%, 250 ml of volume and identical shape, were generated. The size of the uncompressed phantoms was 170 mm in vertical direction, 100 mm in lateral direction and 50 mm in chest wall-nipple direction. For each phantom, both the adaptive mesh and the homogeneous mesh were created using Simpleware® with the following characteristics:

- *Adaptive mesh*: 5 mm as maximum edge length of the tetrahedron and 0.5 mm as minimum.
- *Homogeneous mesh*: the length of the tetrahedron edges was

set to be 1 mm.

In addition, the quality of the tetrahedra of both meshes was maintained as high as possible by means of the parameters that Simpleware® provides for that purpose. This way, the size of the adaptive meshes was in the order of 900 000 elements and 180 000 nodes. On the other hand, the homogeneous meshes were formed by 425 000 elements and 90 000 nodes. The same homogeneous mesh was used for all the phantoms since the differences among the meshes only corresponded to the difference of the internal tissue assignation. Figure 4.14 shows the same slice of both the adaptive mesh and the homogeneous mesh for the same phantom. The smoothness in the boundaries between dense and fatty tissue is noticeable for the adaptive mesh while the homogeneous mesh shows a sharper contour. However, the homogeneous mesh shows more regular elements and, therefore, elements of higher quality. On the other hand, the adaptive mesh presents more distorted and lower quality elements, especially in the boundaries between tissues.

In order to make comparable the results obtained for each deformed phantom, both meshes, the adaptive mesh and the homogeneous mesh, were constructed so that the mesh quality coefficients mentioned in Section 4.4.1 presented similar values for both of them. This was possible for all the coefficients except for coefficient M_5. The reason is that M_5 is related to the homogeneity of the mesh, thus being impossible to achieve a similar value for both meshes since the elements of the adaptive meshes had different sizes and shapes all over the volume. Figure 4.15 shows the average values obtained by the aforementioned mesh quality

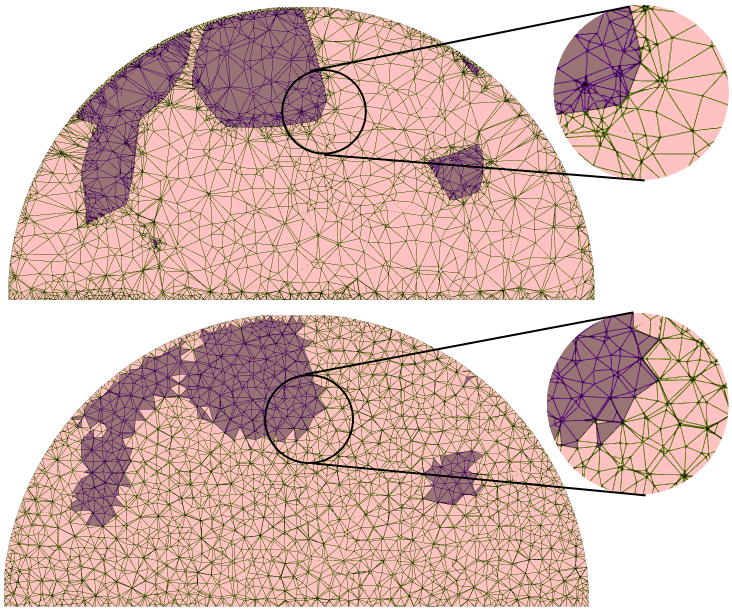

Figure 4.14: *Slice of the adaptive mesh (top) and corresponding slice of the homogeneous mesh (bottom) of the same phantom. Dark color represents the glandular tissue and clear color represents the fat tissue.*

coefficients. The figure compares how the quality of the adaptive mesh is dependent of the minimum edge length of the elements, from 3 mm to 1 mm as well as the quality of the mesh without any restriction in the edge length (non-refined mesh). Furthermore, all tetrahedra of the constructed meshes had an average aspect ratio below 10. The reason was that a tetrahedron is considered as a bad element if its aspect ratio is equal or greater than 10 [Hibbitt and Sorensen, 2001]. This, along with the aforementioned mesh quality coefficients, ensured enough quality in all meshes to make comparable their performance in the simulation of the mammo-

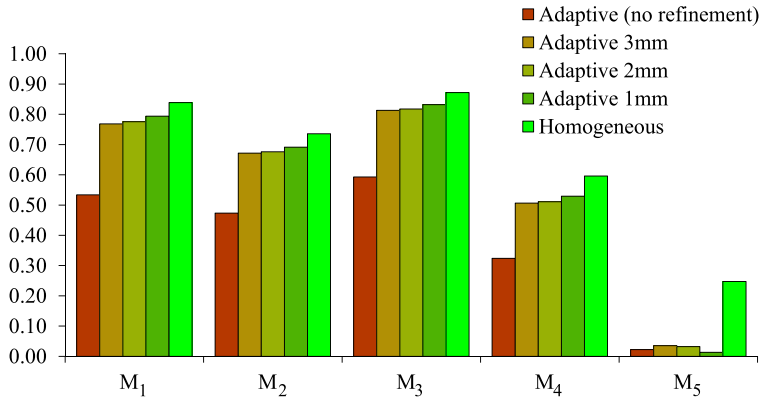

Figure 4.15: *Value of the five quality measures for different mesh sizes including the non-refined adaptive mesh without any edge length restriction (first bar), adaptive mesh with different minimum edge lengths (3 mm, 2 mm, and 1 mm) and the homogeneous mesh (last bar). All the measures have a range between 0 and 1, with 1 being the highest quality.*

Table 4.2: *Average and worst aspect ratios for the adaptive mesh and the homogeneous mesh for all the phantoms.*

	average	worst
adaptive	1.70	8.86
homogeneous	1.55	5.33

graphic compression due to an X-ray mammography. Table 4.2 shows the average aspect ratio for both adaptive and homogenous mesh.

The simulation of the mammographic compression was performed using FEBio, an open source software for solving nonlinear finite element equations in biomechanical applications [Maas et al., 2012]. The used computer was an Intel Xeon X5650 @ 2.66 GHz (12 cores) with 64GB of RAM. The average time consumed by FEBio to solve every simulation using either the adaptive mesh and the

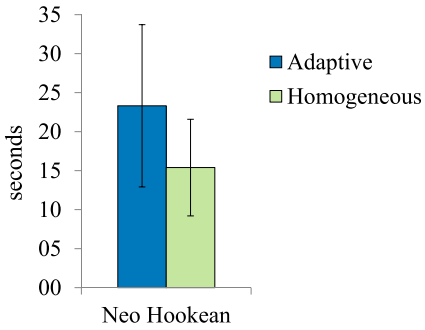

Figure 4.16: *Average time needed to solve the deformation for every 1000 elements and standard deviation.*

homogeneous mesh was also measured. Figure 4.16 shows the average time required to obtain the deformation for every 1000 elements in the CC direction.

The comparison of the deformed phantoms was carried out using only the dense tissue compartments. The large number of fat compartments could cause the average values to be less significant. Moreover, the majority of the differences were present in the neighborhood of dense tissue compartments, hence, the focus was made on these areas. Table 4.3 shows the results of the comparison of the deformed phantoms for both CC compression (top row) and MLO compression (bottom row), respectively. Values of the similarity coefficients reported in Section 3.3 are provided for both simulations in this table. Additionally, Figure 4.17 shows a visual comparison of the same slice from a deformed phantom using an adaptive mesh and a homogeneous mesh.

Finally, the last step in the generation of phantom mammograms consists in the simulation of the X-ray projection through

Table 4.3: *Comparison between the homogeneous mesh and the adaptive mesh using a neo-Hookean model for dense compartments in CC and MLO compression for 10 phantoms.*

	cent. dist.	vol. diff.	JC	MHD
CC	2.54 vox	1759.4 vox	0.8257	1.1792 vox
MLO	0.2683 vox	197.9 vox	0.8723	1.2772 vox

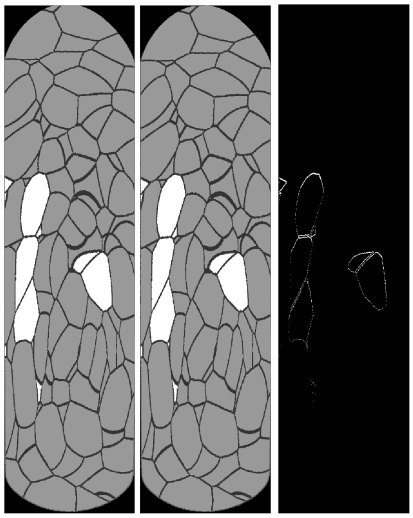

Figure 4.17: *Corresponding slices of the same deformed raw phantom using an adaptive mesh (left), a homogeneous mesh (middle) and their absolute differences (right).*

the deformed phantom. The projections were simulated using the ray tracing algorithm, assuming the ideal (point) focal spot, polyenergetic X-ray beam without scatter and an ideal detector model. The X-ray quantum noise and the electronic noise were simulated by adding two Poisson distributed random processes. Figure 4.18 shows a projection of the same phantom deformed using the adaptive mesh and the homogeneous mesh and their signed differences. The signed differences show dark and white

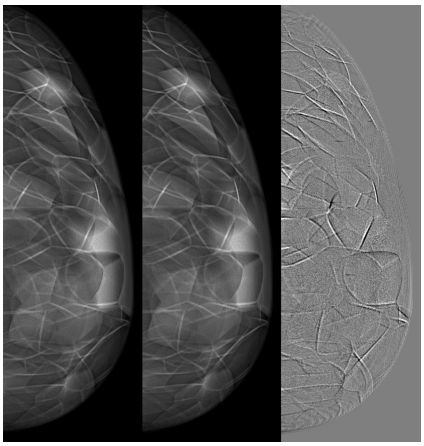

Figure 4.18: *X-Ray mammographic projection of the same phantom using adaptive mesh (left), homogeneous mesh (right) and their absolute differences (right). Gray pixels indicate equal values in the images while black and white pixels indicate the differences.*

values for differing pixels of the adaptive mesh and homogeneous mesh models respectively. Gray values correspond to identical pixels.

4.4.4 Discussion

All similarity coefficients used to compare the adaptive meshes and the homogeneous meshes showed that the difference was mostly in the size of the compartments (Table 4.3). Bearing in mind that the phantom resolution was 200 µm, the average distance between compartment centroids was 0.508 mm (2.54 voxels) in the CC compression while in the MLO compression, the difference was 0.05 mm (0.2683 voxels). On the other hand, the average volume difference was 14.08 mm^3 (1759.4 voxels) and 1.58 mm^3

(197.9 voxels), respectively. Considering that the volume of the original phantom is 250 000 mm^3, these differences represent less than a 0.0065% of the total volume.

A value of Jaccard Coefficient of approximately 0.8 indicates that the overlap was not complete because of the small size of some compartments. In these cases, a displacement of a few voxels could cause JC to move to low values. The JC values increased quickly if these compartments were ignored. Nevertheless, MHD presented very low values, approximately 0.24 mm (1.2 voxels) for CC and MLO compression. Taking into account that the compression was from 100 mm to 50 mm in CC and the voxel size was 200 µm, differences of less than 1 mm between compartments can be neglected. It is important to highlight that the values of the similarity coefficients were better in MLO compression than in CC compression since the breast is subjected to a higher deformation in CC than in MLO.

In order to know how much influence the chosen biomechanical model had on the results, an identical study was performed using the Mooney-Rivlin hyperelastic model proposed by [Tanner et al., 2006b]. In this case, results showed an average distance between compartment centroids comparing adaptive mesh versus homogeneous mesh of 0.66 mm in CC and 0.17 mm in MLO while the difference in volume was 16.3 mm^3 in CC and 2.63 mm^3 in MLO. The chosen model does not make any difference between both meshing types since the Mooney-Rivlin model provided similar results to the neo-Hookean model. Both models have proved their suitability to simulate the mammographic compression for real cases [Gefen and Dilmoney, 2007; del Palomar et al., 2008;

Rajagopal et al., 2008; Chung et al., 2008; Shih et al., 2010].

Regarding the time needed for the simulation of the mammographic compression, the homogeneous mesh presented much faster convergence than the adaptive mesh. For the adaptive mesh, the solution needed, on average, approximately 23 seconds per 1000 elements and in the case of the homogeneous mesh, the time needed per 1000 elements was 15 seconds. Given that the elements of the homogeneous mesh were more regular, their solving times were much shorter than the time needed to solve the problem using the adaptive mesh. This was one of the main consequences of having an irregular mesh, the time needed to get the solution increases with the number of bad-quality tetrahedra. The standard deviation of the time points out the great impact that the mesh quality had in the solver and, therefore, in the solution. The average total time for deforming the adaptive meshes in CC direction was around 7 hours while for the homogeneous meshes was around 2 hours, having both of them similar quality and providing virtually identical results. For the MLO compression, the average total time was 2 hours for deforming the adaptive mesh and 1.45 hours for the homogeneous mesh.

Even though one of the main advantages of the adaptive mesh is to need less elements, the number of elements in the adaptive mesh after the refinement was much higher than the number of elements in the homogeneous mesh. This was due to the difficulty of constructing an automatic adaptive mesh with good quality elements, especially in the regions between tissues. Generating the adaptive mesh with less elements resulted in a considerable reduction of the quality of the tetrahedra thus providing an un-

reliable solution when compared to the solution with the homogeneous mesh. On the other hand, the unconstrained nature of the homogeneous mesh resulted in sharp boundaries between tissues. The homogeneous mesh is only an approximation to the real boundaries but this becomes a trade-off: increasing the number of elements would make the elements of the mesh closer to the real tissue distribution but it would also increase the time needed to solve the FEM.

Finally, figures 4.17 and 4.18 confirm that the differences between the deformed phantom and its projection using the adaptive mesh and the homogeneous mesh are mostly in the surroundings of the glandular compartments. The random noise added to the projections is the responsible of the rough texture present in the projection difference.

In summary, the homogeneous meshes are more adequate to perform the simulation of the mammographic compression for a pipeline of synthetic mammograms generation. The homogeneous meshes provided the same degree of accuracy than the adaptive meshes independently of the model chosen to represent the biomechanical behavior of the breast tissues but with shorter computational times [Lago et al., 2013b].

Using homogeneous meshes in an automatic pipeline of breast mammogram simulations can speed up the generation of samples without losing accuracy since they do not need manual intervention to be repaired and polished. This may lead to a fast automatic pipeline of virtual mammogram generation starting with the phantom creation and ending with the simulated X-ray projection.

4.5 Biomechanical modeling of the breast tissues

There are many models proposed to simulate the breast tissue behavior. The most simplistic models considered the breast as a homogeneous tissue [Carter et al., 2008]. Roose et al., 2006 used an elastic model to simulate the breast behavior, however, for large deformations, the soft tissue presents hyperelastic behavior [Rajagopal et al., 2008]. The work in [Ruiter et al., 2006] compared different elastic and hyperelastic models in order to simulate the mammographic compression, they concluded that the anisotropy of the breast due to the internal tissue distribution must be considered for simulating this compression. Additionally, simplifying the breast model without considering the internal tissues may lead to unrealistic simulations and that approximation could cause overestimation on the X-ray dose with the resultant overestimation of the risk for the patient [Sechopoulos et al., 2012].

To accurately model the breast biomechanical behavior, the response of the three main internal tissues must be modeled: fat, glandular tissue and skin. For that reason, other works reported heterogeneous models of the breast [Azar et al., 2001; Samani and Plewes, 2004; del Palomar et al., 2008; Pathmanathan et al., 2008; Solves Llorens et al., 2012].

On the other hand, even though most biomechanical models of the breast do not include the anisotropy of the Cooper's ligaments due to the difficulty of knowing their location, some sensitivity studies consider that their influence is significant [Tanner et al., 2006b; Ruiter et al., 2006; Gefen and Dilmoney, 2007]. Therefore,

the effect of Cooper's ligaments must be taken into account by the model. Furthermore, it must be considered that the breast is always subjected to a force in every acquisition technique due to some loading condition such as gravity or compression. How to obtain the non-deformed state of the breast (the state without loads) is something that is still under investigation [Rajagopal et al., 2010].

The anisotropic hyperelastic model proposed in [Han et al., 2012] assumes that, due to the presence of Cooper's ligaments, as well as the effect of gravity, the behavior of the breast tissues is anisotropic and can be considered as a fiber-reinforced material. This was the model used to test the methodology proposed in this thesis.

4.5.1 Hyperelastic anisotropic model of the breast

According to Han et al., 2012, the orientation of the fibers was defined in the chestwall-nipple direction. This means that the breast is more likely to deform in the fiber direction. This fiber reinforcement allows the simulation of the initial deformation of the breast due to gravity and considers the internal interactions of the Cooper's ligaments [Han et al., 2012]. The strain energy function for materials with fibers aligned in a specific direction can be defined as Eq. 4.6 shows, where the isotropic component W_{iso} and the fiber anisotropy W_{fib} are decomposed.

$$W = W_{iso}(I_1, I_2, I_3) + W_{fib}(I_4) \tag{4.6}$$

Following the indications by Han et al., 2012, a neo-Hookean hyperelastic model was chosen for modeling the behavior of the breast internal tissues. Eq. 4.7 shows the final energy function of the model used in this work.

$$\begin{aligned} W_{iso}(I_1, I_2, I_3) &= \frac{\mu}{2}(I_1 - 3) + \frac{1}{d}(J-1)^2 \\ W_{fib}(I_4) &= \frac{\eta}{2}(I_4 - 1)^2 \end{aligned} \tag{4.7}$$

where μ stands for the initial shear modulus of the material, d stands for the incompressibility parameter of the material, η stands for a parameter controlling the strength of the fibers, and J stands for the determinant of the deformation gradient tensor.

Both μ and d parameters can be determined from other two elastic parameters, the Young's modulus E and the Poisson's ratio ν as it is shown in Eq. 4.8.

$$\begin{aligned} \mu &= \frac{E}{2(1+\nu)} \\ d &= \frac{2}{k} \\ k &= \frac{E}{3(1-2\nu)} \end{aligned} \tag{4.8}$$

The skin was considered isotropic with only one parameter to estimate, E_{skin}. Finally, and assuming that all the tissues are incompressible ($\nu = 0.49$), $\langle E_{fat}, \eta_{fat}, E_{glandular}, \eta_{glandular}, E_{skin} \rangle$ was the set of parameters to be estimated by the search algorithm.

4.5.2 Estimation of the biomechanical properties

The application of the methodology developed for the *in-vivo* estimation of the biomechanical behavior for the breast is based on the acquisition by an MRI-guided biopsy device of two 3D images of the breast in different states of deformation. The description of the MRI-guided biopsy was detailed in Section 4.2.2. This device can provide an MRI of the free breast in prone position and another MRI of the breast subjected to a controlled compression produced by the plates that keep the breast in a fixed position during the biopsy. In the last case, the applied compression force must be known in order to perform the virtual simulation of that compression. The compression force can be provided by the MRI-guided biopsy device by means of a force detector placed on the plates as described in [Tan et al., 2010].

From the MRI of the uncompressed breast, the simulation of the compression produced by the plates was performed using the proposed biomechanical model. Then, an iterative search process is applied in order to find the elastic constants of the constitutive equations of the proposed model, trying to provide the best fit between the simulated compressed MRI and the real compressed MRI.

The methodology uses the parameter optimization based on genetic heuristics described in Section 3.2 with the GSF as the fit function. The simulation was carried out applying the FEM to a breast software phantom to simulate the compression on synthetic cases. The use of phantoms allowed to have realistic scenarios while controlling all the constraints as well as reducing the amount

of unknown boundary conditions. Since the biomechanical model needs the distribution of the different tissues of the breast, it is assumed that this segmentation can be performed as described in [Solves Llorens et al., 2012].

4.5.3 Software phantom generation

The breast phantoms used in this work were proposed by Pokrajac et al., 2012. They are formed by three materials: fat tissue, glandular tissue and skin. The effect of the Cooper's ligaments was modeled by the anisotropy of the proposed biomechanical model as described in Section 4.5.1. The generation of the phantoms was carried out by recursive partitioning using octrees and implemented on GPUs in order to speed up the process [Chui et al., 2012]. The breast phantoms consisted of a 3D raw volume simulating the distribution of fat and dense compartments in the breast volume separated by the Cooper's ligaments and wrapped by the skin (Section 4.3, Figure 4.10). The breast phantoms were constructed using the homogeneous meshes as described in Section 4.4.

4.5.4 Boundary conditions and contact

The mesh of the breast phantom was placed between two rigid plates, thus simulating the breast compression in an MRI biopsy device (Figure 4.19). Additionally, the corresponding nodes belonging to the chest wall were restricted in the chestwall-nipple direction (Z) and the nodes already in contact with the fixed plate were also restricted in the vertical direction (X) to avoid rigid body

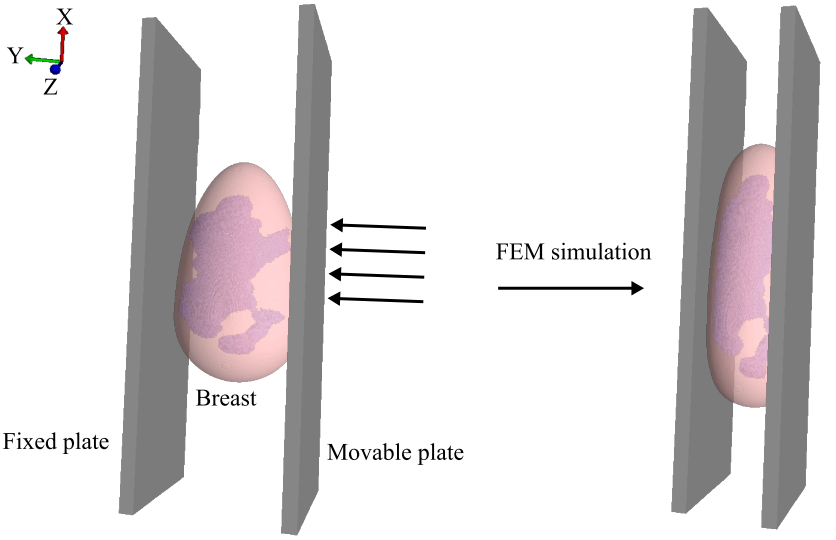

Figure 4.19: *Simulation of the mammographic compression of a breast phantom in an MRI-guided biopsy device.*

displacement during the simulation. A force F was applied to the movable plate in the Y direction while the other plate was completely fixed. To reduce the variability of the experiment and the number of variables affecting the whole simulation, the contact between the plates and the breast surface was modeled as a non-friction contact.

4.5.5 Search algorithm

A diagram of the iterative search algorithm used to estimate the biomechanical parameters of the proposed model is shown in Figure 4.20. A genetic heuristic was used in order to drive the search as it was described in Section 3.2. First, the breast compression was simulated using the target set of parameters $\mathbf{X_t}$.

This simulation was used as a ground truth in order to evaluate the similarity of each candidate simulation.

The iterative search algorithm works as follows: in each generation i of the algorithm, the candidate sets of parameters $\mathbf{X}_i$ are applied to the model to simulate the breast compression. Both the target deformation and the candidate simulation are used to deform the 3D software phantom, thus having a target phantom and a candidate phantom. The creation of the deformed phantoms was carried out on the GPU, considering the undeformed phantom as a 3D texture and using a linear interpolation of the gray levels over each deformed element of the mesh.

The comparison was carried out only on the glandular tissue compartments and using the Geometric Similarity Function (GSF), described in Section 3.3, as the fit function. The larger size of fat tissue with regard to glandular tissue could cause the average values of GSF to be less significant. Additionally, the main differences were located in the neighborhood of glandular tissue compartments. Therefore, the focus was made on those areas even though the fat tissue may be considered as well to perform the volume comparison or even to validate the results with a different measure.

4.5.6 Results

Ten phantoms with glandular density randomly distributed between 7% and 35%, with a volume of 250 ml and identical shape were generated. For all of them, the size of the uncompressed phantoms was 170 mm in vertical direction, 100 mm in lateral

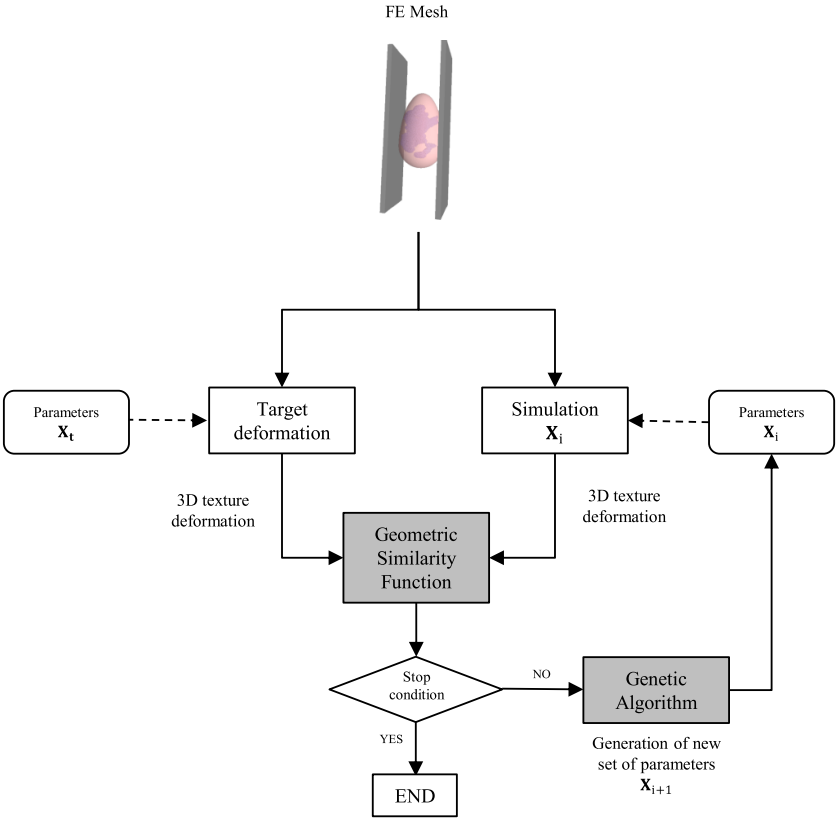

Figure 4.20: *Flowchart of the optimization process using genetic heuristics.*

direction and 50 mm in chestwall-nipple direction. The resolution of the phantom voxel was set to be 200 µm, which was small enough to detect the slightest differences between candidate and target deformations.

A uniformly distributed force F of 100 N was applied to the movable plate. This value was chosen as the average value of the forces applied to perform mammographic compression to real patients during X-ray mammography [Solves Llorens et al., 2012].

The experiment considered three different sets of target parameters. Two experiments, named $\mathbf{X_t^1}$ and $\mathbf{X_t^2}$, in which the skin tissue was not considered and was treated as fat tissue were performed. The first two experiments simplified the model to prove the methodology considering different breast tissue behaviors. A third experiment $\mathbf{X_t^3}$ was also carried out, this time taking into account the skin, thus having a complete model of the breast.

Target and predicted parameters for each one of the phantoms are shown in Tables 4.4, 4.5 and 4.6. The stop condition for all the experiments was triggered when the fit function did not improve more than 10^{-6} in the last 5 generations. It is important to notice that even though GSF is very useful to discriminate good and bad volume similarity, there is no natural interpretation of its values. Therefore, the tables show the values of JC and MHD for interpretation purposes.

Considering the variability of the biomechanical behavior of glandular and fat tissues estimated by Han et al., 2012, the search space of the iterative algorithm was defined by the following

initial intervals:

$$\begin{aligned} E_{fat} &\in [5000 - 20000] \text{ Pa} \\ \eta_{fat} &\in [50000 - 200000] \\ E_{glandular} &\in [5000 - 80000] \text{ Pa} \\ \eta_{glandular} &\in [50000 - 200000] \\ E_{skin} &\in [200000 - 3000000] \text{ Pa} \end{aligned}$$

The genetic algorithm configuration was set up as follows: the population size for each iteration was set to 84 in order to parallelize the process among the 12 cores of the computer. The crossover fraction was set to 0.8, this meant that the 20% of the children were generated by mutation and the 80% by crossover; the elite count was set to 2. Finally, the number of generations was set to 15, ensuring enough exploration of the search space in a reasonable computation time. This configuration was previously analyzed in [Martínez-Martínez et al., 2013b]. Taking advantage of the independent simulations of the genetic algorithm within the same generation, the process was parallelized in the different cores of the computer thus accelerating the search.

In this experiment, the commercial FE package ANSYS® was used to simulate the target deformation as well as each candidate simulation. The glandular compartments of the candidate compressed phantoms were compared with the same compartments of the target compressed phantom with the GSF as the fit function using the implemented genetic algorithm in MATLAB® [Chipperfield and Fleming, 1995]. The number of simulations needed to

Table 4.4: *Parameters for the target deformation* $\mathbf{X_t^1}$ *and estimated parameters for the model without skin.*

	E_{fat} (Pa)	η_{fat}	$E_{glandular}$ (Pa)	$\eta_{glandular}$	JC	MHD (vox)
$\mathbf{X_t^1}$	**10 000**	**100 000**	**40 000**	**150 000**	1	0
$\hat{\mathbf{X}}_\mathbf{t}^\mathbf{1}$ Phantom 1	9746	107 720	49 812	119 410	0.947	0.689
$\hat{\mathbf{X}}_\mathbf{t}^\mathbf{1}$ Phantom 2	10 036	104 840	40 049	126 520	0.988	0.20
$\hat{\mathbf{X}}_\mathbf{t}^\mathbf{1}$ Phantom 3	9766	119 430	47 541	114 900	0.944	0.788
$\hat{\mathbf{X}}_\mathbf{t}^\mathbf{1}$ Phantom 4	10 086	113 560	37 552	110 840	0.978	0.422
$\hat{\mathbf{X}}_\mathbf{t}^\mathbf{1}$ Phantom 5	10 303	91 353	40 256	60 956	0.913	0.90
Avg. $\hat{\mathbf{X}}_\mathbf{t}^\mathbf{1}$	9987	107 381	43 042	106 525	-	-
Std. Dev.	234	10 569	5314	26 130	-	-
Error	1.83 %	10.84 %	10.05 %	28.98 %	-	-

achieve the final values varied between phantoms and was about 1000 simulations in 48h of computation time. The used computer was an Intel Xeon X5650 @2.66 GHz (12 cores) with 64GB of RAM.

Figure 4.21 shows one section of the same phantom deformed using the target parameters (left) and the estimated parameters (middle). Additionally, the right image shows their absolute differences, white pixels denote the non matching pixels between the target and estimated deformed phantom.

4.5.7 Discussion

The first two experiments (Table 4.4 and Table 4.5) achieved a mean relative error of 1.83% and 4.77% for E_{fat}, 10.05% and 5.40% for $E_{glandular}$, and 10.84% and 12.79% for η_{fat}. These errors are relatively low and the estimation of these parameters with the pre-

Table 4.5: *Parameters for the target deformation* $\mathbf{X_t^2}$ *and estimated parameters for the model without skin.*

	E_{fat} (Pa)	η_{fat}	$E_{glandular}$ (Pa)	$\eta_{glandular}$	JC	MHD (vox)
$\mathbf{X_t^2}$	**7500**	**75 000**	**30 000**	**112 500**	1	0
$\hat{\mathbf{X}}_\mathbf{t}^\mathbf{2}$ Phantom 6	7538	73 112	29 826	121 820	0.991	0.226
$\hat{\mathbf{X}}_\mathbf{t}^\mathbf{2}$ Phantom 7	6785	96 682	31 488	154 810	0.926	0.667
$\hat{\mathbf{X}}_\mathbf{t}^\mathbf{2}$ Phantom 8	7523	95 324	28 292	74 674	0.953	0.652
$\hat{\mathbf{X}}_\mathbf{t}^\mathbf{2}$ Phantom 9	6520	75 593	34 445	180 770	0.923	0.850
$\hat{\mathbf{X}}_\mathbf{t}^\mathbf{2}$ Phantom 10	7532	71 527	29 717	99 797	0.988	0.258
Avg. $\hat{\mathbf{X}}_\mathbf{t}^\mathbf{2}$	7180	82 448	30 754	126 374	-	-
Std. Dev.	490	12 468	2353	42 330	-	-
Error	4.77 %	12.79 %	5.40 %	30.30 %	-	-

Table 4.6: *Parameters for the target deformation* $\mathbf{X_t^3}$ *and estimated parameters for the model considering the skin.*

	E_{fat} (Pa)	η_{fat}	E_{gland} (Pa)	η_{gland}	E_{skin} (Pa)	JC	MHD (vox)
$\mathbf{X_t^3}$	**10 000**	**100 000**	**40 000**	**150 000**	**1 600 000**	1	0
$\hat{\mathbf{X}}_\mathbf{t}^\mathbf{3}$ Ph. 1	10 086	101 290	37 390	160 110	1 577 800	0.933	0.72
$\hat{\mathbf{X}}_\mathbf{t}^\mathbf{3}$ Ph. 2	10 116	102 534	69 040	159 300	1 492 338	0.91	2.29
$\hat{\mathbf{X}}_\mathbf{t}^\mathbf{3}$ Ph. 3	9886	84 556	40 958	87 594	1 637 200	0.961	1.71
$\hat{\mathbf{X}}_\mathbf{t}^\mathbf{3}$ Ph. 4	11 372	87 682	30 150	165 830	1 502 500	0.949	1.18
$\hat{\mathbf{X}}_\mathbf{t}^\mathbf{3}$ Ph. 5	11 452	77 835	40 307	191 230	1 499 500	0.90	1.29
Avg. $\hat{\mathbf{X}}_\mathbf{t}^\mathbf{3}$	10 369	92 845	37 817	155 159	1 572 020	-	-
Std. Dev.	1029	14 076	4503	39 549	69 689	-	-
Error	7.95 %	12.82 %	7.00 %	20.08 %	4.56 %	-	-

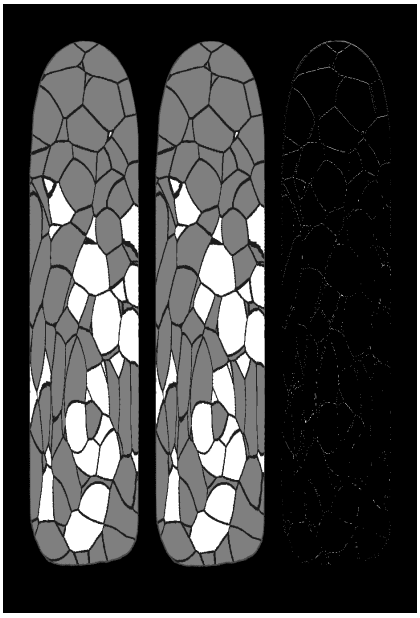

Figure 4.21: *Left: Coronal section of the deformed phantom using the target parameters* $\mathbf{X}_{\mathbf{t}}^{\mathbf{1}}$. *Middle: Coronal section of the deformed phantom with the estimated parameters. Right: Difference between target and estimated deformed phantoms. In the right image, white pixels correspond to mismatching voxels.*

sented methodology can be considered successful. Regarding the parameter controlling the fiber strength for the glandular tissue, $\eta_{glandular}$, its estimation was not so accurate.

To analyze this result, a sensitivity analysis was performed in order to know the influence of this parameter in the model. To perform this, all the parameters except $\eta_{glandular}$ were fixed to their target values. Then, $\eta_{glandular}$ was iterated separately over the search interval [50 000 - 200 000] and the deformed phantom obtained with this set of parameters was compared to the target phantom. Figure 4.22 shows a graph with the tendency of JC

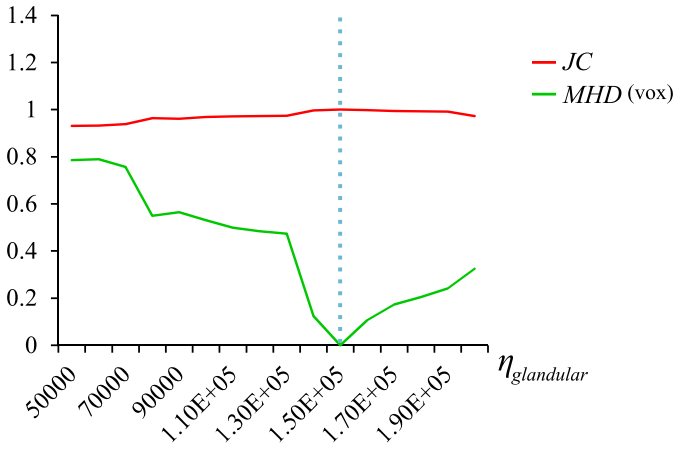

Figure 4.22: *Sensitivity test over the glandular tissue. JC and MHD in terms of $\eta_{glandular}$. The dotted line is the corresponding value to the target phantom.*

and MHD when varying $\eta_{glandular}$ over the initial search interval. Values of JC>0.93 and MHD<1 voxels in the whole range proved the low influence of this parameter in the model.

The η parameters take into account two effects: gravity force and influence of Cooper's ligaments. On one hand, the breast is subjected to initial strains-stresses due to the gravity force in both states, compressed and uncompressed. Ideally, the deformation caused by the gravity force must be considered separately of the tissue constitutive model. Unfortunately, knowing the non-strain state of the breast is something that is still being investigated [Rajagopal et al., 2008]. On the other hand, the influence of the Cooper's ligaments was modeled only in one direction as stated in [Han et al., 2011]. Since they have an unknown effect on the model, the effect of these ligaments should be better modeled in the three directions of the space. This would involve that new

parameters were added to the model. Nevertheless, they could also be estimated with the proposed methodology.

Regarding the anisotropic parameter for the fat tissue, η_{fat}, its estimation was more accurate with an error lower than 13%. This discrepancy with the estimation of $\eta_{glandular}$ may be due to the higher presence of fat tissue in the breast as well as the higher influence of the Cooper's ligaments in this tissue. This results in a higher effect of η_{fat} on the model compared to the effect of $\eta_{glandular}$.

It is important to highlight the importance of JC and MHD, which indicate how accurate the estimation was. The best estimated set of parameters were for Phantoms #2 and #6, where the JC value was about 0.99 and the MHD value was 0.2 voxels (1 vox = 200 µm). These are good indicators of the accuracy of the estimated parameters which, especially in these cases, were very close to the target parameters with errors lower than 1% for E_{fat} and $E_{glandular}$ and lower than 5% for η_{fat}.

As for the estimation of the whole model of the breast, including the skin, the accuracy of the elastic parameters showed errors lower than 8% (Table 4.6). The addition of the skin to the model did not decrease the performance of the methodology. In this case, the estimated elasticity for the skin was achieved with a 4.56% of relative mean error which indicates a great influence in the breast model as reported in [Solves Llorens et al., 2012]. On the other hand, the estimation of the η parameters showed an accuracy in consonance with the first two experiments, where $\eta_{glandular}$ did not induce much variability within the search range.

The number of elements of the FE mesh also influenced the search algorithm. Increasing the element density would impact highly the time needed to solve the contact problem but would also increase the accuracy of the search. Furthermore, reducing the search intervals would cause the algorithm to converge faster by reducing the search space. In this paper, those intervals were set particularly wide in order to prove the suitability of the methodology in case of barely knowing the elastic parameters of the different tissues. Moreover, increasing the complexity of the problem by using a biomechanical model with more parameters would cause the algorithm to converge slower. Nevertheless, the methodology could still be applied since genetic heuristics are very efficient to handle problems with many variables to optimize.

The application of the methodology to real breasts should consider additional factors such as segmentation discrepancies, the heterogeneity of the same tissue type along the breast and the presence of the pectoral muscle. Despite the higher complexity of the internal distribution of the breast tissues, the MRI can be segmented as detailed in [Solves Llorens et al., 2012] and the comparison between the real compressed MRI and each candidate biomechanical model can follow the same procedure. In order to know the accuracy of the estimation of the parameters in real cases, the values of JC and MHD can be analyzed. The closer JC is to 1 and MHD is to 0, the more accurate the estimated parameters of the model are.

4.6 Conclusions

The estimation of the biomechanical parameters of the breast tissues was performed using a software phantom which generated the anatomy of the breast allowing the simulation of the breast compression in an MRI-guided biopsy device. Furthermore, the quality of the finite element mesh used for modeling the breast internal tissues was analyzed. Homogeneous meshes proved to perform better for the simulation of the mammographic compression. This type of mesh is able to accelerate the finite element simulation and provides more stability.

The application of the proposed methodology to the breast may allow the *in-vivo* estimation of the patient-specific biomechanical properties of the breast internal tissues. The tissues were this way characterized by the determination of the elastic constants of an anisotropic hyperelastic model for the fat and glandular tissues and for an isotropic elastic model in the case of the skin.

The genetic algorithm was able to find a set of elastic constants almost identical to the target ones without knowing anything about the original behavior and in a wide search space. The performance of the methodology was proved with breast phantoms achieving an estimation error of less than 10%.

The methodology to characterize the constitutive model of real breasts would follow the same procedure. The 3D MRI image of a controlled compression of the breast on the MRI-guided biopsy device can be used as a target deformation and the MRI image of the uncompressed breast can be used to perform the search.

However, in the case of real breasts, there are some external variables that should be taken into account as boundary conditions such as the variability of the biomechanical behavior of the same tissue within the breast, segmentation errors, the gravity effect, the position of the breast in the device or the attachement to the pectoral muscle.

Chapter 5

Characterization of the biomechanical behavior of the cornea

This chapter presents a methodology for the *in-vivo* estimation of the elastic constants specific for the patient of the biomechanical model that characterize the human cornea. The Corvis® ST device was used to obtain a video sequence of the cornea deformation. Using the images of the deformed cornea from this sequence, a search algorithm iterates over the elastic constants to simulate a deformation as close as possible to the real deformed cornea. The methodology was applied to 24 different corneas from 12 volunteer patients estimating the hyperelastic behavior of the corneal tissue specific for each eye of each patient [Lago et al., 2014b].

5.1 Cornea anatomy

The cornea is the most external part of the ocular globe and protects the eye from external interactions. It has a shape of a regular concave-convex lens and, with approximately 43 diopters, has the highest optical power of the eye although having a fixed focus. The diameter of the cornea is about 12 mm and its thickness is between 400 µm and 600 µm, being thiner in the center than in the periphery. The cornea is attached to the sclera in its periphery.

The human cornea is formed by five layers as it is shown in Figure 5.1. From the most exterior layer to the most interior layer, they are:

- Corneal epithelium: the only layer which is in contact with the air, protecting the rest of layers.
- Bowman's Layer: this layer of about 14 µm is made by collagen fibers and protects the corneal stroma.
- Corneal Stroma: the main component of the cornea representing up to a 90% of it. It is made by transparent collagen fibers in different parallel layers. The orientation of the fibers is mostly in vertical and horizontal directions in the center and following the circumference in the border. This orientations confer the cornea an anisotropic behavior.
- Descemet's Membrane: the base of the corneal endothelium is this acellular membrane of about 10 µm of thickness also made by collagen fibers.

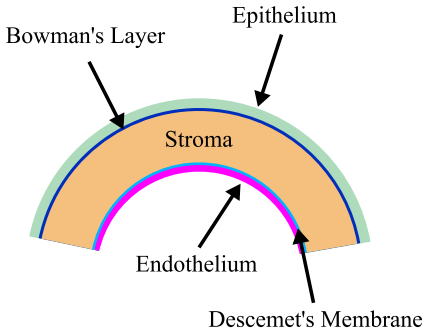

Figure 5.1: *Schematic of the layers of the cornea.*

- Corneal Endothelium: the interior surface of the cornea is covered by this layer of about 5 µm of thickness. This layer is in charge of the impediment of external bodies entering the ocular globe and of the nutrition of the rest of the cornea, since it is not vascularized.

5.2 Biomechanical model of the cornea

The human cornea is considered to be an anisotropic, hyperelastic and incompressible tissue [Elsheikh et al., 2007]. Many different models have been presented in the literature so far [Kaliske, 2000; Dupps and Wilson, 2006; Lanchares et al., 2008; Nguyen et al., 2008; Pandolfi et al., 2009; Studer et al., 2010]. Even though each one has its own benefits, all of them rely on the estimation of the biomechanical parameters that define the model. Most of them have measured these parameters using *ex-vivo* human corneas from an eye bank [Wollensak et al., 2003; Elsheikh et al., 2007]. Others, however, have used the material properties of animal corneas also estimated *ex-vivo* [Ahearne et al., 2007; Boyce et al.,

2007]. The algorithm presented in this thesis is able to estimate *in-vivo* the elastic constants of any biomechanical model proposed for the human cornea.

In this work, the human cornea was considered as a homogeneous tissue and a second order hyperelastic Ogden model was chosen since it provides enough complexity to prove the methodology without disregarding its realism. In addition, this model has been proved to be suitable to simulate the biomechanical behavior of soft tissues. In particular for the behavior of the liver [Martínez-Martínez et al., 2013b].

The energy potential function of the N-order Ogden model is defined in Eq. 5.1.

$$W_O = \sum_{i=1}^{N} \frac{\mu_i}{\alpha_i}(\overline{\lambda}_1^{\alpha_i} + \overline{\lambda}_2^{\alpha_i} + \overline{\lambda}_3^{\alpha_i} - 3) + \sum_{i=1}^{N} \frac{K_{0_i}}{2}(J-1)^{2i} \tag{5.1}$$

where N stands for the order; μ_i and α_i stand for the elastic parameters; $\overline{\lambda}_1$, $\overline{\lambda}_2$ and $\overline{\lambda}_3$ are the deviatoric stretches; K_{0_i} is the Bulk modulus; and J is the determinant of the elastic deformation gradient.

The chosen order for the Ogden model was 2. This ensured enough complexity in the model without detriment of its realism. Note that the coefficient K_{0_i} was fixed to 10^7 Pa thus assuming that the cornea is incompressible [Lanchares et al., 2008]. Therefore, the parameters to be estimated in the model for the cornea were the following: $\langle \mu_1, \alpha_1, \mu_2, \alpha_2 \rangle$.

5.3 Estimation of the biomechanical properties

The methodology presented here relies on the simulation of the deformation of the cornea when applying an air jet for measuring the IOP. This process is known as non-contact tonometry. The Corvis® ST device presented in Section 2.3 was used in the ophtalmologic clinic *Fisabio Oftalmología Médica* to take images of the cornea during the air pressure loading, thus obtaining a sequence of images from the initial state, passing through the state of maximum deformation, and eventually ending in an undeformed state. The simulation of the cornea deformation was performed using the Finite Element Method (FEM), which has been proved to be suitable for large deformations [Glass et al., 2008; Lanchares et al., 2008]. Both segmentation and meshing of the cornea were performed using a MATLAB® script, which also controlled the subsequent iterative search algorithm.

A 2D finite element mesh was constructed from the initial 2D slice using 6-node triangles (Figure 5.2). The nodes of the mesh corresponding to the edge of the peripheral cornea were restricted in all directions representing the anchoring with the sclera, which is thought to be 5 times stiffer than the cornea. The air jet was applied at the apex of the cornea with an average force of 15 mmHg and an estimated diameter of 3 mm, according to the manufacturer's indications.

Additionally, the state of maximum deformation of the cornea was taken from the high-speed video after the air jet application. The deformed cornea was segmented in order to compare the biomechanical simulation of its deformation with the real one.

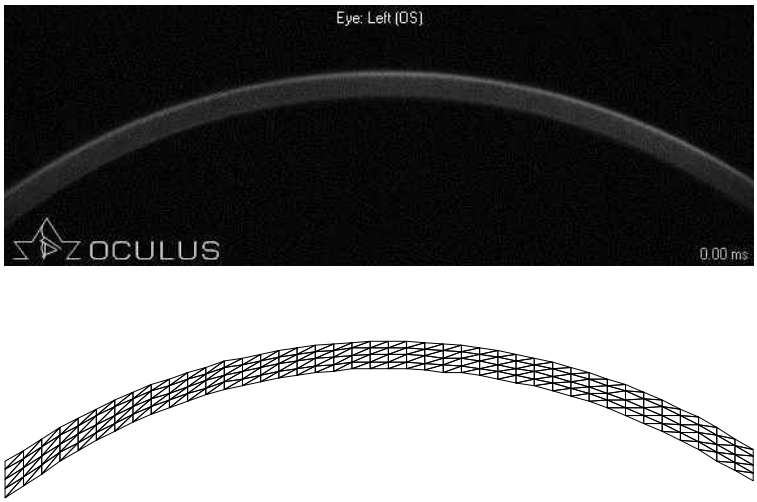

Figure 5.2: *Meshing of the cornea from the 2D image*

Since the initial state of the cornea is actually subjected to the IOP and cannot be considered to be an undeformed state, the first step was to reproduce the deformed state due to the IOP by estimating the initial stresses to which the cornea is subjected. This process is independent of the tonometer used to measure the IOP. It is also independent of the deformation of the cornea caused by the air jet and it was performed before its simulation. After the deformed cornea was segmented, the initial stresses were extracted by the iterative algorithm within the parameter search. The application of the initial stresses on the biomechanical model resulted in the initial state of the cornea. Then, the air jet was applied at the center of the cornea with the corresponding force and a new FE simulation was performed. This was carried out for each set of parameters proposed by the search algorithm.

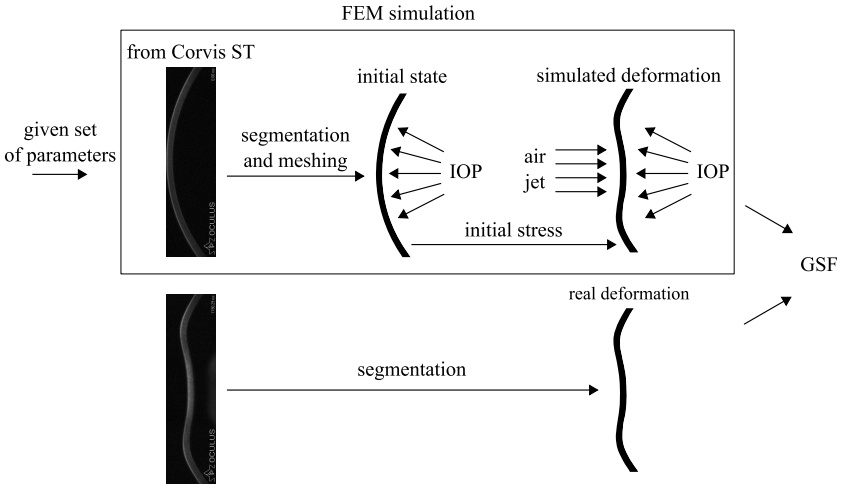

Figure 5.3: *The image of the cornea is segmented and meshed in both deformed and undeformed status. The IOP is applied to the undeformed model in order to obtain the initial stresses that are used to simulate the deformation due to the air jet. Finally, the simulated deformation is compared with the real deformation of the cornea, and the GSF value is retrieved.*

5.4 Search algorithm

The search algorithm uses the parameter optimization methodology as described in Section 3.2. In this case, the fit function to optimize was the dissimilarity of the simulated deformed cornea and the real deformed cornea. The difference was calculated using the Geometric Similarity Function (GSF) which was described in Section 3.3, Eq. 3.31.

The methodology for estimating the parameters of the model has three steps: Initialization, Generation and Termination. Figure 5.3 shows the generation step for each candidate set of parameters.

1. *Initialization*: the algorithm generates an initial random population of elastic parameters $\mathbf{X}_0$ within a given interval for each parameter. Additionally, the real deformed cornea is segmented.

2. *Generation*: successive populations $\mathbf{X}_i$ are generated iteratively by means of the following steps:

    i. The initial stress is calculated for each individual set of parameters as follows:

        a. The IOP is applied to the internal surface of the cornea, considering its original state as a non-deformed state.

        b. The FEM simulates this loaded state with the Ogden model and the set of elastic constants estimated in each case by the search algorithm. This way, the stresses in the cornea are extracted.

c. The extracted stresses are applied to the cornea as initial stresses along with the IOP.

d. Steps a., b., and c. are iterated until the displacement of the cornea is negligible.

e. The final stresses are obtained and used as the initial stress state for further deformation.

ii. The air jet is applied to the model with the initial stress, and the FEM is solved using each individual set of parameters.

iii. The GSF between each simulated deformation of the cornea and the real deformation is evaluated in the current population.

iv. The best individual sets are selected and tagged as parents. Additionally, the best parents are selected as elite.

v. Children are generated both by combining parents (crossover) or by changing a parent randomly (mutation).

vi. A new population is generated by joining children and elite.

3. *Termination*: step 2 is iterated until a stop condition is triggered.

The stop condition can be from a maximum number of iterations, a sensitivity test between two iterations, or a timer. The parameters that achieve the best GSF value $\hat{\mathbf{X}}$, which corresponds to the deformation that is the most similar to the real one, are designated as the estimated parameters of the biomechanical model.

As well as in the case of the breast, the genetic algorithm implemented in MATLAB® was used for the iterative search [Chipperfield and Fleming, 1995]. The search was parallelized in the cores of the computer to accelerate the process.

5.5 Results

First, a synthetic experiment was performed in order to prove the methodology. The same cornea was deformed with two target sets of elastic constants of the biomechanical model. The target sets were $\mathbf{X_1} : \langle \mu_1 = 11000, \alpha_1 = 30, \mu_2 = 35000, \alpha_2 = 80 \rangle$ and $\mathbf{X_2} : \langle \mu_1 = 36000, \alpha_1 = 50, \mu_2 = 32500, \alpha_2 = 88 \rangle$. Their selection was arbitrary within a previously estimated range. The selection of IOP and pachymetry was also arbitrary, with the values of these variables corresponding to an average value among the obtained data of all the patients. The search algorithm was launched in order to find these given sets of parameters. Table 5.1 shows the results for the synthetic experiment for the two corneas, including the target and estimated parameters, JC and MHD values and the mean relative error between them. The genetic algorithm stopped when the 5 last generations were not able to improve the fit function more than 10^{-6}.

Afterward, 24 samples from 12 patients with healthy cornea between the ages of 25 and 40 years old were used to apply the methodology. These patients were volunteers who gave informed consent. The deformations of the corneas were registered by the Corvis® ST device, and the specific value of the IOP and the pachymetry were measured for each cornea. The size of the pixels

Table 5.1: *Target (Tg.), estimated parameters (Est.) and mean relative error (RE) for the synthetic experiment.*

	IOP (mmHg)	Pachy. (µm)	μ_1 (Pa)	α_1	μ_2 (Pa)	α_2	JC	MHD (µm)
Tg. $\mathbf{X_1}$	10.5	595	**11 000**	**30**	**35 000**	**80**	-	-
Est. $\hat{\mathbf{X}}_\mathbf{1}$			10 711	31.32	33 751	82.44	0.99	4.6
RE (%)	-	-	2.63	4.4	3.6	3.05	-	-
Tg. $\mathbf{X_2}$	10.5	595	**36 000**	**50**	**32 500**	**88**	-	-
Est. $\hat{\mathbf{X}}_\mathbf{2}$			34 031	50.07	32 694	89.71	0.99	4.8
RE (%)	-	-	5.47	0.14	0.6	1.94	-	-
Mean RE (%)	-	-	4.05	2.27	2.1	2.5	-	-

of the Corvis® ST images was 2 µm.

Regarding the configuration of the genetic algorithm, the population was established to 84 enable the pararellization among the 12 cores of the computer. The percentage of crossover generated children was set to 80% and set to 20% for mutation and the elite count was 2, which are the MATLAB® default values. The number of generations was 15 since this configuration has provided good results in previous works [Martínez-Martínez et al., 2013b]. In any case, these parameters can be changed in order to customize the algorithm configuration for each patient.

The biomechanical behavior of the 24 corneas were characterized, estimating the elastic constants of each one for the second-order Ogden model. Table 5.2 shows the estimated parameters for the left and right corneas for all of the patients as well as the JC and MHD values and the mean relative error committed.

Table 5.2: *Estimated biomechanical constants for Left and Right eyes for each patient.*

Patient	IOP (mmHg)	Pachy. (µm)	μ_1 (Pa)	α_1	μ_2 (Pa)	α_2	JC	MHD (µm)
$\mathbf{P}_1$	15	533	36 508	71.62	13 220	50.17	0.88	22.6
	12	535	25 239	74.73	15 360	79.10	0.88	23
$\mathbf{P}_2$	11.5	499	38 160	91.73	29 536	83.21	0.87	21.2
	11	520	27 220	82.29	31 040	90.24	0.87	23
$\mathbf{P}_3$	12.5	458	27 261	91.06	29 539	46.53	0.84	30.8
	8.5	479	39 492	96.80	14 822	6.13	0.87	24.4
$\mathbf{P}_4$	12.0	520	30 434	92.28	7327	32.74	0.88	25
	11.5	524	29 588	86.80	31 693	4.37	0.89	19.8
$\mathbf{P}_5$	11.5	580	38 885	77.89	29 141	60.15	0.83	31.4
	11	601	22 120	98.86	13 096	91.94	0.82	32.2
$\mathbf{P}_6$	11	567	24 495	33.37	19 519	80.66	0.88	21.6
	12	568	22 546	74.73	16 950	80.65	0.87	23
$\mathbf{P}_7$	10.5	527	10 978	31.38	33 946	79.82	0.88	21
	9	540	22 921	68.02	20 739	70.84	0.88	21
$\mathbf{P}_8$	13	595	39 721	60.32	14 361	69.21	0.90	19.8
	14	588	27 156	18.03	38 305	80.82	0.89	20.6
$\mathbf{P}_9$	13.5	606	17 503	91.11	32 674	53.86	0.89	21.4
	12.5	613	23 161	91.77	3731	78.22	0.89	21
$\mathbf{P}_{10}$	14	584	26 511	84.26	23 502	37.52	0.90	20.6
	17	596	5119	97.99	34 767	56.81	0.89	19.8
$\mathbf{P}_{11}$	8	513	8458	98.14	27 897	91.71	0.80	41
	8.5	522	30 704	98.98	15 862	43.92	0.79	43.2
$\mathbf{P}_{12}$	12.5	558	12 330	79.19	21 224	83.78	0.83	35.8
	14.5	555	38 327	11.27	32 852	76.47	0.88	24.4
Avg. $\hat{\mathbf{X}}$			26 034	75.11	22 962	63.70	0.87	25.4
Std.Dev.			9960	26.03	9531	25.01	0.03	6.8

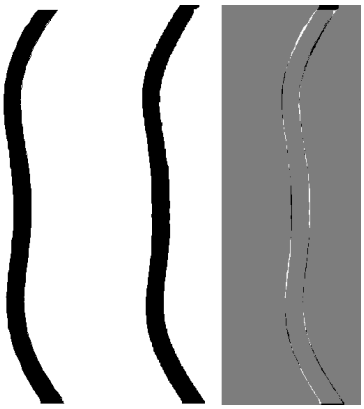

Figure 5.4: *Left: segmentation of the original deformation of a real cornea. Center: simulated deformation of the cornea. Right: signed difference of original and simulated cornea (the gray values are identical in both images; black and white values are signed differences).*

Figure 5.4 shows, for a real experiment, the original segmented cornea, the simulated deformed cornea and their differences for one patient. The gray values identify the correspondence between the two segmentations while the black and white pixels represent the signed differences (positive or negative).

5.6 Discussion

The estimated parameters for the synthetic cases proved that the methodology allows to obtain a biomechanical model that is very similar to the target one. A mean relative error of less than 5% in the estimation of the μ parameters and an error of around 2.5% in the estimation of α parameters indicate a very small deviation from the target parameters. Even though GSF is very useful for performing the iterative search since it considers

both overlap and distance, it is hard to translate its values into a real meaning. Therefore, only JC and MHD values are used to interpret the results. JC showed a value of 0.99 (99% overlap), and MHD showed a maximum distance of less than 5 µm, which indicates that the simulated deformation is virtually identical to the target deformation.

Moving on to the real corneas, the differences between pixels observed in Figure 5.4 show a thin line of non-matching pixels along the surface of the cornea (internal and external). Table 5.2 shows that this distribution of non-matching pixels led to JC values of 87% which means that the majority of the cornea tissue is overlapping. Additionally, having as many white pixels as black pixels indicates that the maladjustment is distributed all along the surface and in the same proportion. On the other hand, the MHD values showed that the distances between the simulated and real deformed cornea were, on average, close to 25 µm (5% of the average corneal thickness) which indicated the great resemblance of the two images. Therefore, the JC and MHD values allow knowing how good the adjustment has been, which gives an idea about the reliability of the estimated model for that specific patient.

The parameters of the Ogden model obtained between individual patients proved to be very different due to the high variability in composition and heterogeneity of the population. Average values of 26034 ± 9960 Pa and 22962 ± 9531 Pa for μ_1 and μ_2, respectively, and 75.11 ± 26.03 and 63.70 ± 25.01 for α_1 and α_2, respectively, are in consonance with previous studies that pointed out this variability [Elsheikh et al., 2007].

Even though an isotropic hyperelastic Ogden model was used to prove the algorithm, the methodology presented here can be used with any other biomechanical model chosen to represent the real behavior of the cornea, even adding more complexity like considering anisotropy or viscoelasticity. The only difference will be the number of parameters that the genetic algorithm has to handle and the consequent computation time necessary.

The Corvis® ST device used for the image acquisition proved to be suitable for this methodology even though more complex personalized devices could be used to characterize the anisotropy or viscoelasticity of the model. This is the only device currently on the market that can provide the information for the *in-vivo* characterization of the human cornea. If more information of the undeformed and deformed cornea (such as a 3D reconstruction or a different type of deformation) were available, this methodology could achieve much more accurate results.

The worst values of JC and MHD appeared in cases where the position of the air jet was not exactly aimed at the apex of the cornea, while, in the simulated model, it is always applied at it. Therefore, the image acquisition must be carefully performed in order to avoid inaccurate and unreliable results. Correcting these abnormalities can lead to greater values of JC (closer to those obtained in the synthetic experiments), which would guarantee a lower error in the parameter estimation.

This methodology was proved to be suitable in a simple 2D model of the cornea. Therefore, having a 3D geometry of the cornea would increase the accuracy of the estimated biomechan-

ical model and it would broaden the applications of having a biomechanical characterization of the corneal tissue. Moreover, with these simulated deformations, additional physiological properties of the cornea could also be inferred.

The elastic parameters of the average cornea may also be useful to construct a generic biomechanical model of the human cornea. Therefore, the average elastic parameters were also used to simulate the air jet and compared with the real deformation of each patient. The results of the simulation with the average cornea led to JC values of 0.536 ± 0.256 and average MHD values of 79.38 ± 163.77 µm which indicates that the average cornea is not useful for every patient.

5.7 Conclusions

In this chapter, the methodology for the *in-vivo* estimation of the elastic constants was applied to model the human corneal tissue. Two experiments were carried out, a synthetic experiment with the aim to prove the performance and evaluate the accuracy of the methodology, and a second experiment with real corneas. The iterative search was able to characterize the biomechanical behavior of the cornea of each patient with a hyperelastic, second-order Ogden model. Twenty-four patient-specific biomechanical models were constructed which proved to be very similar to the real behavior of the patients' corneas.

This methodology is easily applicable to any biomechanical model adding also anisotropy and viscoelasticity. Furthermore, being able to estimate the biomechanical behavior of the cornea

would also allow physiological and optical parameters like hysteresis or refractive power to be inferred, and would also allow the cornea response to be simulated during and after refractive surgical procedures. Additionally, a very interesting line of research would be to classify the cornea behavior taking into account different factors such as gender, age or, ocular diseases.

Chapter 6

Conclusions

This dissertation has presented a methodology for the *in-vivo* characterization the biomechanical behavior of two different organs: the breast and the cornea. The methodology can be translated to construct a biomechanical model for the breast and for the cornea without the need of any invasive intervention, and within the clinical protocols.

The methodology considers the estimation of the elastic constants as a parameter optimization problem. A genetic heuristic was selected to drive the search algorithm due to its ability to find the minimum of a complex function that may present many local minima. The optimization was carried out using, as fit function, a volumetric similarity function, the GSF, which considers both overlap and distance between the real deformation of an organ and its simulation.

6.1 Summary of contributions

- **Selection of the best coefficients for volume comparison**: This experiment tested the behavior of several coefficients used traditionally for validation of segmentations in order to compare the similarity between two volumes. It was proved that the combination of Jaccard Coefficient and the Modified Hausdorff Distance allows the evaluation of the realism of a simulation of the deformation of an organ by its biomechanical model.

- **Mesh quality study**: This study proved the high importance of the quality of the mesh elements in order to get reliable simulations and avoid convergence problems. The use of a homogeneous mesh instead of an adaptive mesh is more suitable to simulate complex internal tissue distributions as can be found in the breast.

- **Biomechanical parameter estimation for the breast tissues**: In the case of the breast, the mammographic compression during an MRI biopsy is able to retrieve the 3D volume of the compressed breast. A biomechanical model simulating the same compression was used to create software phantoms trying to mimic the current procedure. The application of the parameter estimation to the breast phantoms achieved an accuracy of about 90%.

- **Biomechanical parameter estimation for the cornea**: Finally, the parameter estimation was also used to create a biomechanical model of the human cornea taking advantage

of the tonometry. This technique is used to measure the IOP of the eye by applying an air jet to the cornea. The Corvis® ST device records the deformation over time of the cornea. These images were used to create a biomechanical model simulating the air jet. 24 corneas were characterized and a validation with synthetic experiments proved to obtain an accuracy of above 95%.

6.2 Future work

Since the methodology proposed in this thesis was tested, in the case of the breast, with software phantoms, the next step in this research will be to apply it to real patients. First, the breast will be segmented to separate the different internal tissues. The homogeneous meshing algorithm will be used to mesh the complex internal structures such as the glandular tissue thus improving the convergence of the simulation. The force applied by the MRI scanner can be obtained using a force sensor on the compression plates and the simulation of the compression can be performed as it was described for the phantoms. Finally, the iterative search will be able to estimate the elastic constants that define the biomechanical behavior of the breast tissues for each specific patient. This model could be used to locate tumors in different positions of the breasts such as the prone to supine deformation or for the registration between an X-ray mammogram and the MRI.

In the case of the cornea, after estimating the biomechanical behavior of the tissue, some pathologies can be detected since they modify the stiffness of the tissue. Using the 3D reconstruction of

the cornea that can be obtained from devices such as Pentacam together with the biomechanical model previously estimated for the patients the deformation resultant of the insertion of intracorneal rings for patients with keratoconus could be predicted. This way, the position, angle, and ring size will be optimized for each patient. Additionally, some physiological parameters such as the hysteresis or the corneal resistance factor can be estimated.

6.3 Final considerations

The characterization of the behavior of soft tissue is the core of its biomechanical simulation and the responsible of achieving realistic results. With the guarantee of estimating how an organ reacts to external interactions, surgeons can count on having virtual environments capable to simulate real interventions. This way, surgeons can prevent critical scenarios, train their skills, and plan future interventions, as well as use them for surgical guidance.

The development of a complete virtual body that considers all the possible interactions is still far in the future. However, the first steps in this direction are to provide a realistic behavior of the tissues present in the organs. Unfortunately, computational costs are still a big barrier since the time needed for solving the FEM is too high. Even though some meshfree methods are currently gaining popularity in numerical simulation they are still very time consuming [Liu, 2010].

The ultimate goal is the creation of a realistic simulation of the whole human body in real time, but this is something that, to date, is still only in our imagination.

Generated literature

Journal papers

Lago, M. A., Rupérez, M. J., Martínez-Martínez, F., Monserrat, C., Larra, E., Güell, J. L. and Peris-Martínez, C. (2014). A new methodology to in-vivo estimate the elastic constants that characterize the patient-specific biomechanical behavior of the human cornea. *Journal of Biomechanics* (major revisions)

Lago, M. A., Rupérez, M., Martínez-Martínez, F., Bakic, P. R., Maidment, A. D., and Monserrat, C. (2014). Methodology based on genetic heuristics for in-vivo characterizing the patient-specific biomechanical behavior of the breast tissues. *Expert Systems with Applications* (under revision)

International conferences

Lago, M.A., Martínez-Martínez, F., Rupérez, M.J., Monserrat, C., Alcañiz, M. (2012). A study about coefficients to estimate the error in biomechanical models used to virtually simulate the organ behaviors. In *Proceedings of international conference on Medicine Meets Virtual Reality (MMVR)*, volume 173, pages 250–256. IOS Press

Lago, M. A., Martínez-Martínez, F., Rupérez, M., Monserrat, C., and Alcañiz, M. (2012). Breast prone-to-supine deformation and registration using a time-of-flight camera. In *Proceedings of International Conference on Biomedical Robotics and Biomechatronics (BioRob)*, 2012 4th IEEE RAS EMBS, pages 1161–1163.

Lago, M. A., Maidment, A. D., and Bakic, P. R. (2013). Modeling of mammographic compression of anthropomorphic software breast phantom using FEBio. In *Proceedings of International Symposium of Computer Methods in Biomechanics and Biomedical Engineering (CMBBE)*, pages 495–496. This paper obtained the 3rd best student poster award.

Maidment, A. D., Bakic, P. R., Chui, J. H., Avanaki, A. N., Marchessoux, C., Pokrajac, D. D., Espig, K. S., Kimpe, T., Xthona, A., **Lago, M. A.**, and Shankla, V. (2013). The role of virtual clinical trials in preclinical testing of breast imaging systems. In *Proceedings of the 99th Scientific Assembly and Annual Meeting (RSNA)*

Bakic, P. R., Maidment, A. D., Chui, J. H., Avanaki, A. N., Marchessoux, C., Pokrajac, D. D., Espig, K. S., Kimpe, T., Xthona, A., **Lago, M. A.**, and Shankla, V. (2013). Automated and optimized imaging simulation platform for virtual clinical trials of breast cancer screening. In *Proceedings of the 99th Scientific Assembly and Annual Meeting (RSNA)*

Lago, M. A., Rupérez, M., Martínez-Martínez, F., Monserrat, C. (2014). Genetic algorithms for estimating the biomechanical behavior of breast tissues . In *Proceedings of IEEE-EMBS International Conferences on Biomedical and Health Informatics (BHI)*, pages 760–763. This paper obtained the 3rd best student oral communication award.

National conferences

Lago, M. A., Monserrat, C., Rupérez, M. J., Solves-Llorens, J. A., Martínez-Martínez, F., and Alcañiz, M. (2012). Simulación de la deformación de la mama en posición supino partiendo de imágenes de resonancia magnética y usando una cámara Time-of-Flight. In *Proceedings of II Reunión del Capítulo Español de la Sociedad Europea de Biomecánica (ESB)*.

Lago, M. A., Rupérez, M. J., Monserrat, C. (2013). Impact of the Meshing Method in the Biomechanical Simulation of the Mammographic Compression. In *Proceedings of III Reunión del Capítulo Español de la Sociedad Europea de Biomecánica (ESB)*, page 38

Bibliography

Ahearne, M., Yang, Y., Then, K., and Liu, K.-K. (2007). An indentation technique to characterize the mechanical and viscoelastic properties of human and porcine corneas. *Annals of Biomedical Engineering*, 35(9):1608–1616. 2 citations in pages 16 and 97.

Alastrué, V., Calvo, B., Pena, E., and Doblaré, M. (2006). Biomechanical modeling of refractive corneal surgery. *Journal of Biomechanical Engineering*, 128(1):150–160. One citation in page 15.

Aspert, N., Santa-Cruz, D., and Ebrahimi, T. (2002). MESH: measuring errors between surfaces using the Hausdorff distance. In *Proceedings of IEEE International Conference on Multimedia and Expo, ICME '02.*, volume 1, pages 705–708 vol.1. One citation in page 33.

Azar, F. S., Metaxas, D. N., and Schnall, M. D. (2001). A Deformable Finite Element Model of the Breast for Predicting Mechanical Deformations under External Perturbations. *Academic Radiology*, 8(10):965 – 975. One citation in page 76.

Bakic, P. R., Albert, M., Brzakovic, D., and Maidment, A. D. A. (2002). Mammogram synthesis using a 3D simulation. I. Breast tissue model and image acquisition simulation. *Medical Physics*, 29(9):2131–2139. 3 citations in pages 53, 56, and 60.

Bakic, P. R., Ng, S., Ringer, P., Carton, A.-K., Conant, E. F., and Maidment, A. D. A. (2010). Validation and optimization of digital breast tomosynthesis reconstruction using an anthropomorphic software breast phantom. *Proceedings of SPIE*, 7622:76220F–76220F–9. One citation in page 56.

Bakic, P. R., Zhang, C., and Maidment, A. D. A. (2011). Development and characterization of an anthropomorphic breast software phantom based upon region-growing algorithm. *Medical Physics*, 38(6):3165–3176. 5 citations in pages 53, 54, 57, 60, and 146.

Balocco, S., Camara, O., Vivas, E., Sola, T., Guimaraens, L., Gratama van Andel, H. A. F., Majoie, C. B., Pozo, J. M., Bijnens, B. H., and Frangi, A. F. (2010). Feasibility of estimating regional mechanical properties of cerebral aneurysms in-vivo. *Medical Physics*, 37(4):1689–706. One citation in page 31.

Barr, R. G. (2012). Sonographic breast elastography: A primer. *Journal of Ultrasound in Medicine*, 31(5):773–783. One citation in page 13.

Bhatti, S. N. and Sridhar-Keralapura, M. (2012). A novel breast software phantom for biomechanical modeling of elastography. *Medical Physics*, 39(4):1748–1768. 3 citations in pages 55, 56, and 146.

Bianchi, G., Solenthaler, B., Székely, G., and Harders, M. (2004).

Simultaneous topology and stiffness identification for mass-spring models based on FEM reference deformations. In *Proceedings of Medical Image Computing and Computer-Assisted Intervention (MICCAI 2004)*, pages 293–301. Springer, Heidelberg. One citation in page 27.

Billiar, K. and Sacks, M. (2000). Biaxial mechanical properties of the native and glutaraldehyde-treated aortic valve cusp: Part II - A structural constitutive model. *Journal of Biomechanical Engineering-Transactions of the ASME*, 122(4):327–335. One citation in page 10.

Bliznakova, K., Bliznakov, Z., Bravou, V., Kolitsi, Z., and Pallikarakis, N. (2003). A three-dimensional breast software phantom for mammography simulation. *Physics in Medicine and Biology*, 48(22):3699. 3 citations in pages 54, 55, and 146.

Bliznakova, K., Suryanarayanan, S., Karellas, A., and Pallikarakis, N. (2010). Evaluation of an improved algorithm for producing realistic 3D breast software phantoms: Application for mammography. *Medical Physics*, 37(11):5604–5617. One citation in page 54.

Boyce, B., Jones, R., Nguyen, T., and Grazier, J. (2007). Stress-controlled viscoelastic tensile response of bovine cornea. *Journal of Biomechanics*, 40(11):2367–2376. 2 citations in pages 16 and 97.

Bucki, M., Lobos, C., Payan, Y., and Hitschfeld, N. (2011). Jacobian-based repair method for finite element meshes after registration. *Engineering with Computers*, 27(3):285–297. 2 citations in pages 59 and 60.

Burkhart, T. A., Andrews, D. M., and Dunning, C. E. (2013). Finite

element modeling mesh quality, energy balance and validation methods: A review with recommendations associated with the modeling of bone tissue. *Journal of Biomechanics*, 46(9):1477 – 1488. 2 citations in pages 20 and 59.

Cárdenes, R., de Luis-García, R., and Bach-Cuadra, M. (2009). A multidimensional segmentation evaluation for medical image data. *Computer Methods and Programs in Biomedicine*, 96(2):108 – 124. One citation in page 32.

Carter, F. J., Frank, T. G., Davies, P. J., McLean, D., and Cuschieri, A. (2001). Measurements and modelling of the compliance of human and porcine organs. *Medical Image Analysis*, 5(4):231 – 236. One citation in page 11.

Carter, T., Tanner, C., Beechey-Newman, N., Barratt, D., and Hawkes, D. (2008). MR Navigated Breast Surgery: Method and Initial Clinical Experience. In *Medical Image Computing and Computer-Assisted Intervention (MICCAI 2008)*, volume 5242 of *Lecture Notes in Computer Science*, pages 356–363. Springer Berlin Heidelberg. 2 citations in pages 12 and 76.

Chatterjee, S., Laudato, M., and Lynch, L. A. (1996). Genetic algorithms and their statistical applications: an introduction. *Computational Statistics & Data Analysis*, 22(6):633 – 651. One citation in page 27.

Chen, B., Shorey, J., Jr., R. S. S., Richard, S., Thompson, J., Nolte, L. W., and Samei, E. (2011). An anthropomorphic breast model for breast imaging simulation and optimization. *Academic Radiology*, 18(5):536 – 546. One citation in page 54.

Chew, P. H., Yin, F. C., and Zeger, S. L. (1986). Biaxial stress-

strain properties of canine pericardium. *Journal of Molecular and Cellular Cardiology*, 18(6):567 – 578. One citation in page 10.

Chipperfield, A. and Fleming, P. (1995). The MATLAB genetic algorithm toolbox. In *Applied Control Techniques Using MATLAB, IEE Colloquium on*, pages 10/1–10/4. 2 citations in pages 85 and 104.

Chui, J. H., Pokrajac, D. D., Maidment, A. D. A., and Bakic, P. R. (2012). Towards Breast Anatomy Simulation Using GPUs. In *Digital Mammography / IWDM*, pages 506–513. 3 citations in pages 54, 57, and 80.

Chung, J.-H., Rajagopal, V., Nielsen, P. M., and Nash, M. P. (2008). Modelling mammographic compression of the breast. In *Medical Image Computing and Computer-Assisted Intervention (MICCAI 2008)*, pages 758–765. Springer. One citation in page 74.

Clark, R. (1973). Stress-strain characteristics of fresh and frozen human aortic and mitral leaflets and chordae tendineae - implications for clinical use. *Journal of Thoracic and Cardiovascular Surgery*, 66(2):202–208. One citation in page 10.

Cox, M. A., Driessen, N. J., Boerboom, R. A., Bouten, C. V., and Baaijens, F. P. (2008). Mechanical characterization of anisotropic planar biological soft tissues using finite indentation: Experimental feasibility. *Journal of Biomechanics*, 41(2):422 – 429. One citation in page 11.

Cox, S., Mithraratne, K., and Smith, N. (2007). An anatomically based finite element model of the lower limbs in the seated posture. In *Engineering in Medicine and Biology Society, 2007. EMBS*

2007. 29th Annual International Conference of the IEEE, pages 6326–6329. One citation in page 20.

Crum, W. R., Tanner, C., and Hawkes, D. J. (2005). Anisotropic multi-scale fluid registration: evaluation in magnetic resonance breast imaging. *Physics in Medicine and Biology*, 50(21):5153. One citation in page 30.

Curry, T., Dowdey, J., and Murry, R. (1990). *Christensen's Physics of Diagnostic Radiology*. Lea & Febiger. One citation in page 50.

Dance, D. R., Hunt, R. A., Bakic, P. R., Maidment, A. D. A., Sandborg, M., Ullman, G., and Alm Carlsson, G. (2005). Breast dosimetry using high-resolution voxel phantoms. *Radiation Protection Dosimetry*, 114(1-3):359–363. One citation in page 54.

Deenadayalu, C., Mobasher, B., Rajan, S., and Hall, G. (2006). Refractive change induced by the LASIK flap in a biomechanical finite element model. *Journal of Refractive Surgery*, 22(3):286–292. One citation in page 15.

del Palomar, A. P., Calvo, B., Herrero, J., López, J., and Doblaré, M. (2008). A finite element model to accurately predict real deformations of the breast. *Medical Engineering and Physics*, 30(9):1089 – 1097. 3 citations in pages 12, 73, and 76.

delBuey, M., Lanchares, E., Cristobal, J., Calvo, B., and Lavilla, L. (2010). Comparative biomechanical analysis of combined treatments for keratoconus. *In proceedings of ASCRS Symposium and Congress.* One citation in page 15.

Dice, L. R. (1945). Measures of the amount of ecologic association

between species. *Ecology*, 26(3):297–302. One citation in page 32.

Diekmann, F., Meyer, H., Diekmann, S., Puong, S., Muller, S., Bick, U., and Rogalla, P. (2009). Thick slices from tomosynthesis data sets: Phantom study for the evaluation of different algorithms. *Journal of Digital Imaging*, 22(5):519–526. One citation in page 54.

Dubuisson, M. P. and Jain, A. K. (1994). A modified Hausdorff distance for object matching. In *Proceedings of 12th International Conference on Pattern Recognition*, pages 566–568. IEEE Comput. Soc. Press. 2 citations in pages 35 and 39.

Dupps, W. J. and Wilson, S. E. (2006). Biomechanics and wound healing in the cornea. *Experimental Eye Research*, 83(4):709 – 720. One citation in page 97.

Edelsbrunner, H. (2001). *Geometry and Topology for Mesh Generation*. Cambridge. One citation in page 62.

Egan, R. (1988). *Breast Imaging: Diagnosis and Morphology of Breast Diseases*. W. B. Saunders. One citation in page 46.

Elsheikh, A., Wang, D., Brown, M., Rama, P., Campanelli, M., and Pye, D. (2007). Assessment of corneal biomechanical properties and their variation with age. *Current Eye Research*, 32(1):11–19. 4 citations in pages 15, 16, 97, and 108.

Field, D. (2000). Qualitative Measures for Initial Meshes. In *International Journal of Numerical Methods in Engineering*, volume 47, pages 887–906. One citation in page 62.

Fogel, D. (1995). *Evolution Computation: Toward a New Philosophy of*

Machine Intelligence. Press, Piscataway, NJ. One citation in page 26.

Fung, Y. (1972). Stress-Strain-History Relations of Soft Tissues in Simple Elongation. In *Biomechanics: Its Foundations and Objectives*. Prentice-Hall, Englewood Cliffs, NJ. One citation in page 9.

Fung, Y. (1974). Biorheology of loose connective tissues, especially blood vessels. In *Biopolymere und Biomechanik von Bindegewebssystemen*, pages 191–210. Springer Berlin Heidelberg. One citation in page 10.

Fung, Y. C. (1993). *Biomechanics: Mechanical Properties of Living Tissues*. Hardcover, Springer US. One citation in page 20.

Gee, M. W., Förster, C., and Wall, W. A. (2010). A computational strategy for prestressing patient-specific biomechanical problems under finite deformation. *International Journal for Numerical Methods in Biomedical Engineering*, 26(1):52–72. One citation in page 11.

Gefen, A. and Dilmoney, B. (2007). Mechanics of the normal woman's breast. *Technology and Health Care*, 15(4):259–271. 6 citations in pages 13, 20, 47, 64, 73, and 76.

Gefen, A., Shalom, R., Elad, D., and Mandel, Y. (2009). Biomechanical analysis of the keratoconic cornea. *Journal of the Mechanical Behavior of Biomedical Materials*, 2(3):224 – 236. One citation in page 15.

Ghista, D. and Rao, A. (1973). Mitral-valve mechanics - stress-strain characteristics of excised leaflets, analysis of its functional

mechanics and its medical application. *Medical & Biological Engineering*, 11(6):691–702. One citation in page 10.

Glass, D. H., Roberts, C. J., Litsky, A. S., and Weber, P. A. (2008). A viscoelastic biomechanical model of the cornea describing the effect of viscosity and elasticity on hysteresis. *Investigative Ophthalmology and Visual Science*, 49(9):3919–3926. 2 citations in pages 16 and 99.

Goldmann, H. and Schmidt, T. (1957). Über Applanationstonometrie. *Ophthalmologica*, 134(4):221–242. One citation in page 17.

Gow, B. S. and Vaishnav, R. N. (1975). A microindentation technique to measure rheological properties of the vascular intima. *Journal of Applied Physiology*, 38(2):344–350. One citation in page 11.

Greenleaf, J. F., Fatemi, M., and Insana, M. (2003). Selected methods for imaging elastic properties of biological tissues. *Annual Review of Biomedical Engineering*, 5(1):57–78. One citation in page 13.

Han, L., Hipwell, J., Mertzanidou, T., Carter, T., Modat, M., Ourselin, S., and Hawkes, D. (2011). A hybrid FEM-based method for aligning prone and supine images for image guided breast surgery. In *IEEE International Symposium on Biomedical Imaging: From Nano to Macro*, pages 1239–1242. 3 citations in pages 12, 58, and 89.

Han, L., Hipwell, J. H., Tanner, C., Taylor, Z., Mertzanidou, T., Cardoso, J., Ourselin, S., and Hawkes, D. J. (2012). Development of patient-specific biomechanical models for predicting large

breast deformation. *Physics in Medicine and Biology*, 57(2):455. 7 citations in pages 14, 20, 46, 61, 77, 78, and 84.

Han, L., Noble, J., and Burcher, M. (2003). A novel ultrasound indentation system for measuring biomechanical properties of in-vivo soft tissue. *Ultrasound in Medicine & Biology*, 29(6):813 – 823. One citation in page 11.

Harb, N., Labed, N., Domaszewski, M., and Peyraut, F. (2011). A new parameter identification method of soft biological tissue combining genetic algorithm with analytical optimization. *Computer Methods in Applied Mechanics and Engineering*, 200(4):208 – 215. 2 citations in pages 13 and 20.

Hausdorff, F. (1962). *Set theory, 2nd Ed.* Chelsea Pub. Co. One citation in page 33.

Hesselink, J. R. (2006). Basic Principles of MR Imaging. *Online*. One citation in page 50.

Hibbitt, K. and Sorensen (2001). *ABAQUS/CAE User's Manual*. Hibbitt, Karlsson & Sorensen, Incorporated. One citation in page 68.

Hjortdal, J. Ø. (1995). Extensibility of the normo-hydrated human cornea. *Acta Ophthalmologica Scandinavica*, 73(1):12–17. One citation in page 15.

Hori, R. and Mockros, L. (1976). Indentation tests of human articular cartilage. *Journal of Biomechanics*, 9(4):259 – 268. One citation in page 11.

Hsu, C. M. L., Palmeri, M. L., Segars, W. P., Veress, A. I., and III, J. T. D. (2011). An analysis of the mechanical parameters used

for finite element compression of a high-resolution 3D breast phantom. *Medical Physics*, 38(10):5756–5770. 2 citations in pages 12 and 20.

Humphrey, J., Halperin, H., and Yin, F. (1991). Small indentation superimposed on a finite equibiaxial stretch implications for cardiac mechanics. *Journal of Applied Mechanics-Transactions of the ASME*, 58(4):1108–1111. One citation in page 11.

Huttenlocher, D., Klanderman, G., and Rucklidge, W. (1993). Comparing images using the Hausdorff distance. *IEEE Transactions on Pattern Analysis and Machine Intelligence*, 15(9):850–863. One citation in page 33.

Jeffrey, B. E. (2004). Static Indentation of Anisotropic Biomaterials Using Axially Asymmetric Indenters—a Computational Study. *Journal of Biomechanical Engineering*, 126(4):498–505+. One citation in page 11.

Joe, B. (1991). GEOMPACK - a software package for the generation of meshes using geometric algorithms. *Advances in Engineering Software*, 13:325–331. One citation in page 62.

Johns, P. C. and Yaffe, M. J. (1987). X-ray characterisation of normal and neoplastic breast tissues. *Physics in Medicine and Biology*, 32(6):675. One citation in page 49.

Jong, K. A. (2006). *Evolutionary computation: a unified approach*. MIT Press. One citation in page 26.

Kaliske, M. (2000). A formulation of elasticity and viscoelasticity for fibre reinforced material at small and finite strains. *Computer*

Methods in Applied Mechanics and Engineering, 185(4):225 – 243. One citation in page 97.

Kellner, A. L., Nelson, T. R., Cerviño, L. I., and Boone, J. M. (2007). Simulation of mechanical compression of breast tissue. *Transactions on Biomedical Engineering*, 54(10):1885–91. One citation in page 59.

Kim, J. and Srinivasan, M. (2005). Characterization of viscoelastic soft tissue properties from in-vivo animal experiments and inverse FE parameter estimation. *Medical Image Computing and Computer-Assisted Intervention (MICCAI 2005)*, pages 599–606. One citation in page 20.

Kotecha, A., Elsheikh, A., Roberts, C. R., Zhu, H., and Garway-Heath, D. F. (2006). Corneal thickness- and age-related biomechanical properties of the cornea measured with the ocular response analyzer. *Investigative Ophthalmology and Visual Science*, 47(12):5337–5347. One citation in page 16.

Krouskop, T. A., Wheeler, T. M., Kallel, F., Garra, B. S., and Hall, T. (1998). Elastic moduli of breast and prostate tissues under compression. *Ultrasonic Imaging*, 20(4):260–274. One citation in page 13.

Lago, M., Martínez-Martínez, F., Rupérez, M., Monserrat, C., and Alcañiz, M. (2012a). A study about coefficients to estimate the error in biomechanical models used to virtually simulate the organ behaviors. In *Proceedings of International Conference on Medicine Meets Virtual Reality*, volume 173, pages 250–256. IOS Press. One citation in page 34.

Lago, M. A., Maidment, A. D., and Bakic, P. R. (2013a). Modeling

of mammographic compression of anthropomorphic software breast phantoms using FEBio. In *Proceedings of International Symposium of Computer Methods in Biomechanics and Biomedical Engineering*, pages 495–496. One citation in page 58.

Lago, M. A., Martinez-Martinez, F., Ruperez, M., Monserrat, C., and Alcaniz, M. (2012b). Breast prone-to-supine deformation and registration using a Time-of-Flight camera. In *Proceedings of International Conference on Biomedical Robotics and Biomechatronics (BioRob), 2012 4th IEEE RAS EMBS*, pages 1161–1163. One citation in page 58.

Lago, M. A., Monserrat, C., Rupérez, M. J., Solves-Llorens, J. A., Martínez-Martínez, F., and M., A. (2012c). Simulación de la deformación de la mama en posición supino partiendo de imágenes de resonancia magnética y usando una cámara time-of-flight. In *Proceedings of II Reunión del Capítulo Español de la Sociedad Europea de Biomecánica (ESB)*. One citation in page 58.

Lago, M. A., Rupérez, M. J., Martínez-Martínez, F., and Monserrat, C. (2014a). Genetic algorithms for estimating the biomechanical behavior of breast tissues. In *Proceedings of IEEE-EMBS International Conferences on Biomedical and Health Informatics (BHI)*, pages 760–763. One citation in page 46.

Lago, M. A., Rupérez, M. J., Martínez-Martínez, F., Monserrat, C., Larra, E., Güell, J. L., and Peris-Martínez, C. (2014b). A new methodology to in-vivo estimate the elastic constants that characterize the patient-specific biomechanical behavior of the human cornea (major revisions). *Journal of Biomechanics*. One citation in page 95.

Lago, M. A., Rupérez, M. J., and Monserrat, C. (2013b). Impact of the Meshing Method in the Biomechanical Simulation of the Mammographic Compression. In *Proceedings of Spanish Chapter of the European Society of Biomechanics (ESB)*, page 38. 2 citations in pages 59 and 75.

Lamarque, J. (1984). *An atlas and text of the breast: clinical radiodiagnosis*. Wolfe medical atlases. Wolfe Medical. One citation in page 47.

Lanchares, E., Calvo, B., Cristóbal, J. A., and Doblaré, M. (2008). Finite element simulation of arcuates for astigmatism correction. *Journal of Biomechanics*, 41(4):797 – 805. 5 citations in pages 15, 20, 97, 98, and 99.

Lanir, Y. (1979). A structural theory for the homogeneous biaxial stress-strain relationships in flat collagenous tissues. *Journal of Biomechanics*, 12(6):423 – 436. One citation in page 20.

Lanir, Y. and Fung, Y. (1974). Two-dimensional mechanical properties of rabbit skin II. Experimental results. *Journal of Biomechanics*, 7(2):171 – 182. One citation in page 10.

Lee, A. W. C., Schnabel, J. A., Rajagopal, V., Nielsen, P. M. F., and Nash, M. P. (2010). Breast image registration by combining finite elements and free-form deformations. In *Proceedings of the 10th international conference on Digital Mammography*, IWDM'10, pages 736–743, Berlin, Heidelberg. Springer-Verlag. One citation in page 30.

Li, C. M., Segars, W. P., Tourassi, G. D., Boone, J. M., and Dobbins, J. T. (2009). Methodology for generating a 3D computerized

breast phantom from empirical data. *Medical Physics*, 36(7):3122–3131. 3 citations in pages 54, 55, and 146.

Liu, G. (2010). *Meshfree Methods: Moving Beyond the Finite Element Method, Second Edition*. Taylor & Francis. One citation in page 116.

Lockett, H. and Guenov, M. (2008). Similarity measures for mid-surface quality evaluation. *Computer-Aided Design*, 40(3):368 – 380. One citation in page 33.

Luce, D. A. (2005). Determining in-vivo biomechanical properties of the cornea with an ocular response analyzer. *Journal of Cataract and Refractive Surgery*, 31(1):156 – 162. One citation in page 16.

Ma, A. K. W., Gunn, S., and Darambara, D. G. (2009). Introducing DeBRa: a detailed breast model for radiological studies. *Physics in Medicine and Biology*, 54(14):4533. One citation in page 54.

Maas, S., Ellis, B., Ateshian, G., and Weiss, J. (2012). FEBio: finite elements for biomechanics. *Journal of Biomechanical Engineering*, 134(1):011005. One citation in page 69.

Mariappan, Y. K., Glaser, K. J., and Ehman, R. L. (2010). Magnetic resonance elastography: A review. *Clinical Anatomy*, 23(5):497–511. One citation in page 13.

Martínez-Martínez, F., Lago, M. A., Rupérez, M. J., and Monserrat, C. (2013a). Analysis of several biomechanical models for the simulation of lamb liver behaviour using similarity coefficients from medical image. *Computer Methods in Biomechanics and Biomedical Engineering*, 16(7):747–757. One citation in page 11.

Martínez-Martínez, F., Lago, M. A., Rupérez, M. J., Monserrat, C., Pareja, E., Cortés, M., López, R., and Brugger, S. (2012). A computational method to estimate the elastic parameters of biomechanical models for the in-vivo human liver. In *Proceedings of the 10th International Symposium on Computer Methods in Biomechanics and Biomedical Engineering.*, CMBBE 2012. 2 citations in pages 20 and 42.

Martínez-Martínez, F., Rupérez, M. J., Martín-Guerrero, J. D., Monserrat, C., Lago, M. A., Pareja, E., and López-Andújar, R. (2013b). Estimation of the elastic parameters of human liver biomechanical models by means of medical images and Evolutionary Computation. *Computer Methods and Programs in Biomedicine.* 5 citations in pages 13, 42, 85, 98, and 105.

Matthews, F. and West, J. (1972). Finite element displacement analysis of a lung. *Journal of Biomechanics*, 5(6):591 – 600. One citation in page 58.

May-Newman, K. and Yin, F. (1995). Biaxial mechanical-behavior of excised porcine mitral-valve leaflets. *American Journal of Physiology-Heart and Circulatory Physiology*, 269(4):H1319–H1327. One citation in page 10.

Mehrabian, H., Campbell, G., and Samani, A. (2010). A constrained reconstruction technique of hyperelasticity parameters for breast cancer assessment. *Physics in Medicine and Biology*, 55(24):7489. One citation in page 13.

Miller, K. and Lu, J. (2013). On the prospect of patient-specific biomechanics without patient-specific properties of tissues. *Jour-*

nal of the Mechanical Behavior of Biomedical Materials, 27(0):154 – 166. One citation in page 11.

Mooney, M. (1940). A theory of large elastic deformation. *Journal of Applied Physics*, 11(9):582–592. One citation in page 25.

Nair, A. U., Taggart, D. G., and Vetter, F. J. (2007). Optimizing cardiac material parameters with a genetic algorithm. *Journal of Biomechanics*, 40(7):1646 – 1650. One citation in page 13.

Nava, A., Mazza, E., Furrer, M., Villiger, P., and Reinhart, W. (2008). In-vivo mechanical characterization of human liver. *Medical Image Analysis*, 12(2):203 – 216. One citation in page 11.

Netter, F. (1989). *Atlas of Human Anatomy*. Netter Basic Science. Elsevier Health Sciences. 3 citations in pages 47, 48, and 146.

Nguyen, T. D., Jones, R. E., and Boyce, B. L. (2008). A nonlinear anisotropic viscoelastic model for the tensile behavior of the corneal stroma. *Journal of Biomechanical Engineering*, 130(4). One citation in page 97.

Nielsen, P. M. F., Malcolm, D. T. K., Hunter, P. J., and Charette, P. G. (2002). Instrumentation and procedures for estimating the constitutive parameters of inhomogeneous elastic membranes. *Biomechanics and Modeling in Mechanobiology*, 1(3):211–218. One citation in page 10.

Nishikawa, R., Glick, S., Bakic, P., and Reiser, I. (2011). 3D Breast Models. *Medical Physics*, 38(6):3706–3706. One citation in page 56.

Ogden, R. W. (1972). Large deformation isotropic elasticity: On the correlation of theory and experiment for compressible rubber-

like solids. *Philosophical Transactions of the Royal Society of London. Series A, Mathematical and Physical Sciences*, 328(1575):567–583. One citation in page 25.

O'Hagan, J. J. and Samani, A. (2009). Measurement of the hyperelastic properties of 44 pathological ex vivo breast tissue samples. *Physics in Medicine and Biology*, 54(8):2557. 2 citations in pages 11 and 13.

Ophir, J., Céspedes, I., Ponnekanti, H., Yazdi, Y., and Li, X. (1991). Elastography: A quantitative method for imaging the elasticity of biological tissues. *Ultrasonic Imaging*, 13(2):111 – 134. One citation in page 13.

Pandit, A., Lu, X., Wang, C., and Kassab, G. S. (2005). Biaxial elastic material properties of porcine coronary media and adventitia. *American Journal of Physiology - Heart and Circulatory Physiology*, 288(6):H2581–H2587. One citation in page 13.

Pandolfi, A., Fotia, G., and Manganiello, F. (2009). Finite element simulations of laser refractive corneal surgery. *Engineering with Computers*, 25(1):15–24. 2 citations in pages 15 and 97.

Pathmanathan, P., Gavaghan, D., Whiteley, J., Chapman, S., and Brady, J. (2008). Predicting Tumor Location by Modeling the Deformation of the Breast. *IEEE Transactions on Biomedical Engineering*, 55(10):2471–2480. 2 citations in pages 12 and 76.

Persson, P.-O. and Strang, G. (2004). A Simple Mesh Generator in MATLAB. *SIAM Review*, 46(2):329–345. One citation in page 62.

Pokrajac, D. D., Maidment, A. D. A., and Bakic, P. R. (2012). Optimized generation of high resolution breast anthropomorphic

software phantoms. *Medical Physics*, 39(4):2290–2302. 6 citations in pages 46, 57, 58, 60, 80, and 146.

Provenzano, P. P., Lakes, R. S., Corr, D. T., and Vanderby, R. (2002). Application of nonlinear viscoelastic models to describe ligament behavior. *Biomechanics and Modeling in Mechanobiology*, 1(1):45–57. One citation in page 20.

Ragnemalm, I. (1993). The euclidean distance transform in arbitrary dimensions. *Pattern Recognition Letters*, 14(11):883 – 888. One citation in page 33.

Rajagopal, V., Chung, J.-H., Warren, R., Highnam, R. P., Nash, M. P., and Nielsen, P. M. F. (2006). Finite element modelling of breast biomechanics: Predicting the effects of gravity. In *Computational Biomechanics for Medicine*, MICCAI Workshop, pages 94–103. MICCAI. One citation in page 58.

Rajagopal, V., Lee, A., Chung, J.-H., Warren, R., Highnam, R. P., Nash, M. P., and Nielsen, P. M. F. (2008). Creating individual-specific biomechanical models of the breast for medical image analysis. *Academic Radiology*, 15(11):1425–1436. 4 citations in pages 20, 74, 76, and 89.

Rajagopal, V., Nielsen, P. M. F., and Nash, M. P. (2010). Modeling breast biomechanics for multi-modal image analysis-successes and challenges. *Wiley Interdisciplinary Reviews: Systems Biology and Medicine*, 2(3):293–304. 2 citations in pages 12 and 77.

Richard, F., Bakic, P., and Maidment, A. (2006). Mammogram registration: a phantom-based evaluation of compressed breast thickness variation effects. *IEEE Transactions on Medical Imaging*, 25(2):188–197. One citation in page 54.

Rivlin, R. (1948). Large elastic deformations of isotropic materials. iv. further developments of the general theory. *Philosophical Transactions of the Royal Society of London. Series A, Mathematical and Physical Sciences*, 241(835):379–397. One citation in page 25.

Roose, L., Mollemans, W., Loeckx, D., Maes, F., and Suetens, P. (2006). Biomechanically based elastic breast registration using mass tensor simulation. In *Medical Image Computing and Computer-Assisted Intervention (MICCAI 2006)*, pages 718–725. Springer. One citation in page 76.

Ruiter, N., Stotzka, R., Muller, T.-O., Gemmeke, H., Reichenbach, J., and Kaiser, W. (2006). Model-based registration of X-ray mammograms and MR images of the female breast. *IEEE Transactions on Nuclear Science*, 53(1):204–211. 3 citations in pages 12, 64, and 76.

Samani, A. and Plewes, D. (2004). A method to measure the hyperelastic parameters of ex vivo breast tissue samples. *Physics in Medicine and Biology*, 49(18):4395. 2 citations in pages 11 and 76.

Samani, A. and Plewes, D. (2007). An inverse problem solution for measuring the elastic modulus of intact ex vivo breast tissue tumours. *Physics in Medicine and Biology*, 52(5):1247. One citation in page 20.

Samur, E., Sedef, M., Basdogan, C., Avtan, L., and Duzgun, O. (2005). A robotic indenter for minimally invasive characterization of soft tissues. *International Congress Series*, 1281:713 – 718. CARS 2005: Computer Assisted Radiology and Surgery. One citation in page 11.

Schulz-Wendtland, R., Fuchsjäger, M., Wacker, T., and Hermann, K.-P. (2009). Digital mammography: an update. *European Journal of Radiology*, 72(2):258–265. One citation in page 49.

Sechopoulos, I., Bliznakova, K., Qin, X., Fei, B., and Feng, S. S. J. (2012). Characterization of the homogeneous tissue mixture approximation in breast imaging dosimetry. *Medical Physics*, 39(8):5050–5059. 2 citations in pages 54 and 76.

Shah, S., Laiquzzaman, M., Bhojwani, R., Mantry, S., and Cunliffe, I. (2007). Assessment of the biomechanical properties of the cornea with the ocular response analyzer in normal and keratoconic eyes. *Investigative Ophthalmology and Visual Science*, 48(7):3026–3031. One citation in page 16.

Shi, H., Farag, A., Fahmi, R., and Chen, D. (2008). Validation of Finite Element Models of Liver Tissue Using Micro-CT. *IEEE Transactions on Biomedical Engineering*, 55(3):978–984. 2 citations in pages 20 and 30.

Shih, T.-C., Chen, J.-H., Liu, D., Nie, K., Sun, L., Lin, M., Chang, D., Nalcioglu, O., and Su, M.-Y. (2010). Computational simulation of breast compression based on segmented breast and fibroglandular tissues on magnetic resonance images. *Physics in medicine and biology*, 55(14):4153. 2 citations in pages 64 and 74.

Sinkus, R., Tanter, M., Xydeas, T., Catheline, S., Bercoff, J., and Fink, M. (2005). Viscoelastic shear properties of in-vivo breast lesions measured by MR elastography. *Magnetic Resonance Imaging*, 23(2):159 – 165. One citation in page 13.

Solves Llorens, J., Monserrat, C., Rupérez Moreno, M., Naranjo, V., Alajami, M., Feliu, E., García, M., and Lloret, M. (2012). MRI Skin

Segmentation for the Virtual Deformation of the Breast under Mammographic Compression. In *Proceedings of International Conference on Medicine Meets Virtual Reality*. 8 citations in pages 12, 20, 61, 76, 80, 84, 90, and 91.

Studer, H., Larrea, X., Riedwyl, H., and Büchler, P. (2010). Biomechanical model of human cornea based on stromal microstructure. *Journal of Biomechanics*, 43(5):836 – 842. One citation in page 97.

Studholme, C., Hill, D., and Hawkes, D. (1999). An overlap invariant entropy measure of 3D medical image alignment. *Pattern Recognition*, 32(1):71 – 86. 2 citations in pages 14 and 30.

Tan, U.-X., Yang, B., Gullapalli, R., and Desai, J. (2010). Design and development of a 3-axis MRI-compatible force sensor. In *Robotics and Automation (ICRA), 2010 IEEE International Conference on*, pages 2586–2591. One citation in page 79.

Tanner, C., Carter, T., and D.J., H. (2006a). 3D Rezoning for Finite Element Modelling of Large Breast Deformations. In *Proceedings of European Modelling Symposium*, pages 51–53. 2 citations in pages 12 and 59.

Tanner, C., Schnabel, J. A., Hill, D. L. G., Hawkes, D. J., Leach, M. O., and Hose, D. R. (2006b). Factors influencing the accuracy of biomechanical breast models. *Medical Physics*, 33(6):1758–1769. 2 citations in pages 73 and 76.

Tanner, C., White, M., Guarino, S., Hall-Craggs, M. A., Douek, M., and Hawkes, D. J. (2011). Large breast compressions: Observations and evaluation of simulations. *Medical Physics*, 38(2):682–690. One citation in page 20.

Treloar, L. R. G. (1948). Stresses and Birefringence in Rubber subjected to General Homogeneous Strain. *Proceedings of the Physical Society*, 60(2):135. One citation in page 24.

Ulger, H., Erdogan, N., Kumanlioglu, S., and Unur, E. (2003). Effect of age, breast size, menopausal and hormonal status on mammographic skin thickness. *Skin Research and Technology*, 9(3):284–289. One citation in page 47.

Vieira, M. A. C., Bakic, P. R., and Maidment, A. D. A. (2013). Effect of denoising on the quality of reconstructed images in digital breast tomosynthesis. In *Proceedings of SPIE*, volume 8668, pages 86680C–86680C–14. One citation in page 56.

Vigneron, L. M., Boman, R. C., Ponthot, J. P., Robe, P. A., Warfield, S. K., and Verly, J. G. (2010). Enhanced FEM-based modeling of brain shift deformation in Image-Guided Neurosurgery. *Journal of Computational and Applied Mathematics*, 234(7):2046–2053. 3 citations in pages 20, 31, and 33.

Wollensak, G., Spoerl, E., and Seiler, T. (2003). Stress-strain measurements of human and porcine corneas after riboflavin-ultraviolet-a-induced cross-linking. *Journal of Cataract and Refractive Surgery*, 29(9):1780 – 1785. 2 citations in pages 16 and 97.

Xu, S., Liu, X., and Zhang, H. (2009). Simulation of soft tissue using mass-spring model with simulated annealing optimization. In *Proceedings of the IEEE International Conference on Automation and Logistics*, pages 1543–1547. One citation in page 27.

Yang, H., Christopher, L., Duric, N., West, E., and Bakic, P. (2012). Performance analysis of EM-MPM and K-means clustering in 3D ultrasound image segmentation. In *IEEE International Con-*

ference on Electro/Information Technology (EIT), pages 1–4. One citation in page 56.

Young, S., Bakic, P. R., Myers, K. J., Jennings, R. J., and Park, S. (2013). A virtual trial framework for quantifying the detectability of masses in breast tomosynthesis projection data. *Medical Physics*, 40(5):–. One citation in page 56.

Zeng, Y., Yang, J., Huang, K., Lee, Z., and Lee, X. (2001). A comparison of biomechanical properties between human and porcine cornea. *Journal of Biomechanics*, 34(4):533 – 537. One citation in page 16.

Zhang, J., Joldes, G., Wittek, A., and Miller, K. (2013). Patient-specific computational biomechanics of the brain without segmentation and meshing. *International Journal for Numerical Methods in Biomedical Engineering*, 29(2):293–308. One citation in page 20.

Zhao, X., Raghavan, M., and Lu, J. (2011). Identifying heterogeneous anisotropic properties in cerebral aneurysms: a pointwise approach. *Biomechanics and Modeling in Mechanobiology*, 10(2):177–189. One citation in page 10.

Zheng, Y.-P. and Mak, A. F. T. (1996). An ultrasound indentation system for biomechanical properties assessment of soft tissues in-vivo. *IEEE Transactions on Biomedical Engineering*, 43(9):912–918. One citation in page 11.

Zhou, L., Oldan, J., Fisher, P., and Gindi, G. (2006). Low-contrast lesion detection in tomosynthetic breast imaging using a realistic breast phantom. *Proceedings of SPIE*, 6142:61425A–61425A–12. One citation in page 54.

List of Figures

List of Tables